2014-01-01

Gadolinia Doped Hafnia (gd2o3- Hfo2) Thermal Barrier Coatings For Gas Turbine Applications

Satya Kiran Gullapalli
University of Texas at El Paso, satya6287@gmail.com

GADOLINIA DOPED HAFNIA (Gd_2O_3- HfO_2) THERMAL BARRIER COATINGS FOR GAS TURBINE APPLICATIONS

SATYA KIRAN GULLAPALLI

Environmental Science and Engineering Program

APPROVED:

Ramana V Chintalapalle, Ph.D., Chair

Ahsan R Choudhuri, Ph.D.

Stephen W Stafford, Ph.D.

Yirong Lin, Ph.D.

Jack F Chessa, Ph.D.

Charles Ambler, Ph.D.
Dean of the Graduate School

Dedicated to my parents

GADOLINIA DOPED HAFNIA (Gd_2O_3- HfO_2) THERMAL BARRIER COATINGS FOR GAS TURBINE APPLICATIONS

by

SATYA KIRAN GULLAPALLI, M.S

DISSERTATION

Presented to the Faculty of the Graduate School of

The University of Texas at El Paso

in Partial Fulfillment

of the Requirements

for the Degree of

DOCTOR OF PHILOSOPHY

Environmental Science and Engineering Program

THE UNIVERSITY OF TEXAS AT EL PASO

December 2014

Acknowledgements

I would like to take this opportunity to thank all the individuals who have contributed to the successful completion of this dissertation. Firstly, I am very grateful to my advisor Dr. Ramana Chintalapalle for giving me the opportunity to work on this project. Without his valuable advice and financial support, this work could not have been possible. I would like to thank my co-advisor Dr. Stephen Stafford for all the valuable advice and sharing his expertise with regards to gas turbines. I am thankful to Dr. Jack Chessa for being patient and helping me understand computational modeling. I would like to thank Dr. Ahsan Choudhuri for providing me the financial support in the form of teaching assistantship through the mechanical engineering department during the initial stages of my doctoral program. I would also like to thank Dr. Yirong Lin for agreeing to be on my dissertation committee. I am very grateful to Divi Mangadu and Lisa Yang from Ross Opticals whose advice and resources have greatly contributed to the success of this work. I would like to thank all my research team members Ernesto Rubio, Gustavo Martinez, Mirella Vargas, Juan Gomez and Thomas Joachim for the help and support they have provided during my research. I would also like to thank Armando Delgado, Ricardo Martinez, Mayra Contreras and Brenda Arellano for their help. A special thanks to the people at Micro Materials United Kingdom, for providing us valuable data through their state of the art characterization equipment. Finally, I would like to acknowledge the United States Department of Energy for funding this research.

Abstract

Thermal efficiency of the gas turbines is influenced by the operating temperature of the hot gas path components. The material used for the hot gas path components can only withstand temperature up to a certain limit. Thermal barrier coatings (TBC) provide the additional thermal protection for these components and help the gas turbine achieve higher firing temperatures. Traditionally available yttria stabilized zirconia (YSZ) TBCs have a limitation up to 1200˚ C due to their phase transformation. The present work focuses on gadolinia based hafnia (GSH) TBCs to study their potential to replace the YSZ coatings. Different compositions of gadolinia doped hafnia coatings have been deposited using electron beam physical vapor deposition (EB-PVD) technique and characterized using x-ray diffraction (XRD) and scanning electron microscope (SEM). The crystal structure analysis performed using XRD confirmed the stabilization of the high temperature cubic phase of hafnia. Cross sectional analysis confirmed the presence of columnar structure in the coatings which is a signature of the EB-PVD coatings. Mechanical properties of the coatings were investigated using nanoindentation and nano impact testing at both room temperature and high temperature. Indentation tests indicate a reduction in hardness with an increase in temperature and gadolinia content in hafnia. Impact testing reveals the fracture resistance of the coatings as a function of stabilizer content and heat treatment. Thermal measurements and impedance testing was performed on the bulk material to study the effect of gadolinia content. Thermal cycling was performed to study the spallation behavior of the as deposited and aged samples. Finite element models were developed to study the interfacial stress development in the coatings subjected to thermal cycling.

Table of Contents

List of Tables

List of Figures

Chapter 1: Introduction

Increase in demand for energy, growing concern over global warming due to the use of fossil fuels and the concept of sustainability are the key factors that are currently driving extensive research efforts in renewable energy. However, although there are various forms of renewable energy systems available, none of these have the capability or the efficiency to meet the global current and emerging energy needs when compared to the conventional energy systems. Hence, the scientific and engineering community across the globe has been challenged and focused efforts on further improving the efficiency and economics of the conventional energy systems to meet the ever increasing energy needs.

One of the most commonly used conventional energy system is the coal-based power generation system, where the gas turbines (Figure 1.1) play a key role. The theory of gas turbine was established in the late 18^{th} century but was successfully demonstrated only in 1939 to generate electricity in a power plant. These turbine engines have also been used for aircraft, locomotive and marine applications thereafter. Despite the fact that the turbines find a widespread industrial applications, the efficiency of a single cycle gas turbine is very low. This efficiency loss is usually attributed to the lower turbine temperature, since the efficiency of all types of gas turbines is directly proportional to the turbine inlet temperature. This issue was tackled by improved structural design and airfoil cooling technology applied to higher strength at temperature alloys cast by increasingly complex processes and coated with steadily improved protective systems (1). To improve the efficiency from a materials point of view, thermal barrier coatings (TBCs) are applied to the gas turbine blades. These coatings are low thermal conductivity ceramic refractory materials that protect the gas turbine components from high

temperature and corrosive environment. It has been reported that the application of the TBCs throughout the combustion chamber and on the turbine blades would save an operator around 1-2% of fuel cost translating into savings of over $10 million per annum for some companies (2). A brief history of the evolution of thermal barrier coatings system and their fabrication methods will be discussed ahead.

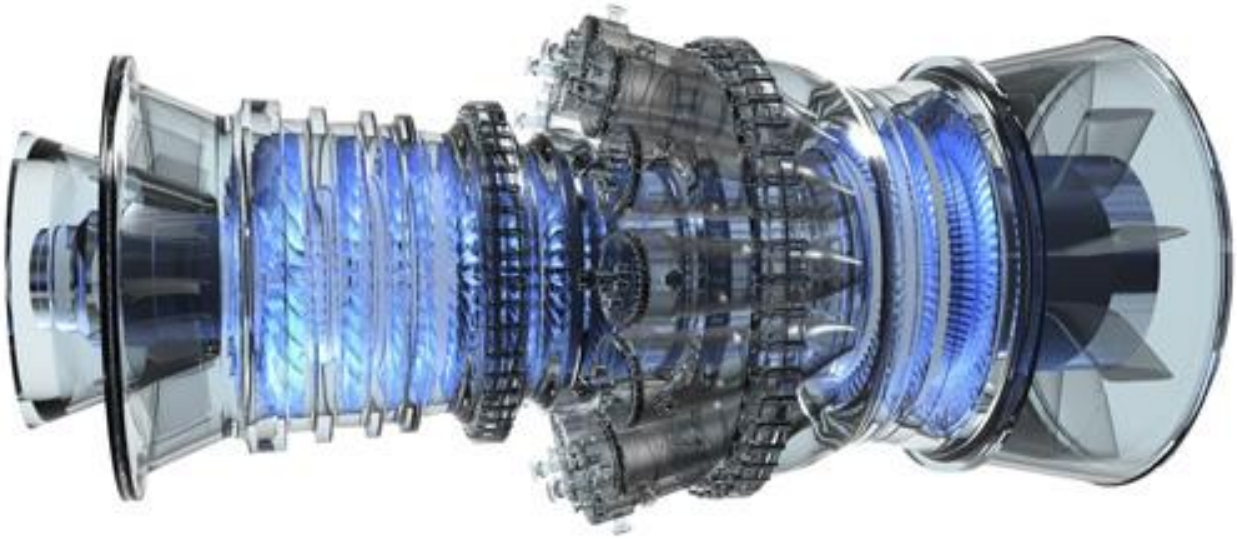

Figure 1.1: GE Frame 7 Gas Turbine [Credit GE]

1.1 History of Thermal Barrier Coatings (TBCs)

The idea of using thermal barrier coatings to protect hot section components was first brought to the front in the United States, by National Aeronautics and Space Administration (NASA) and Air Force research in the late 1950s and early 1960s on thermal control coatings for space vehicles and rocket engines. The first TBC was applied to the NASA X-15 aircraft, where a 10-mil-thick coating of stabilized zirconia over a 5-mil-thick nichrome undercoat. Since then, extensive research was conducted on developing these coatings since they have the potential for increasing the temperature capability of gas turbines by 100-200 °F as indicated in Figure 1.2.

Thermal spray TBCs research was conducted by Sal Grisaffe in the 1960 to understand alumina and zirconia coatings. By 1970s, plasma sprayed TBC were used by Pratt & Whitney (P&W) in low risk aero applications like those in an after burner section. During the mid-70s, TBCs of various yttria doped zirconia compositions on NiCrAlY were developed and tested. Stecura presented an optimum zirconia-yttria TBC composition along with the use of MCrAlY bond coat in 1978 by conducting furnace natural gas torch and burner rig tests as shown in Figure 1.3 (3).

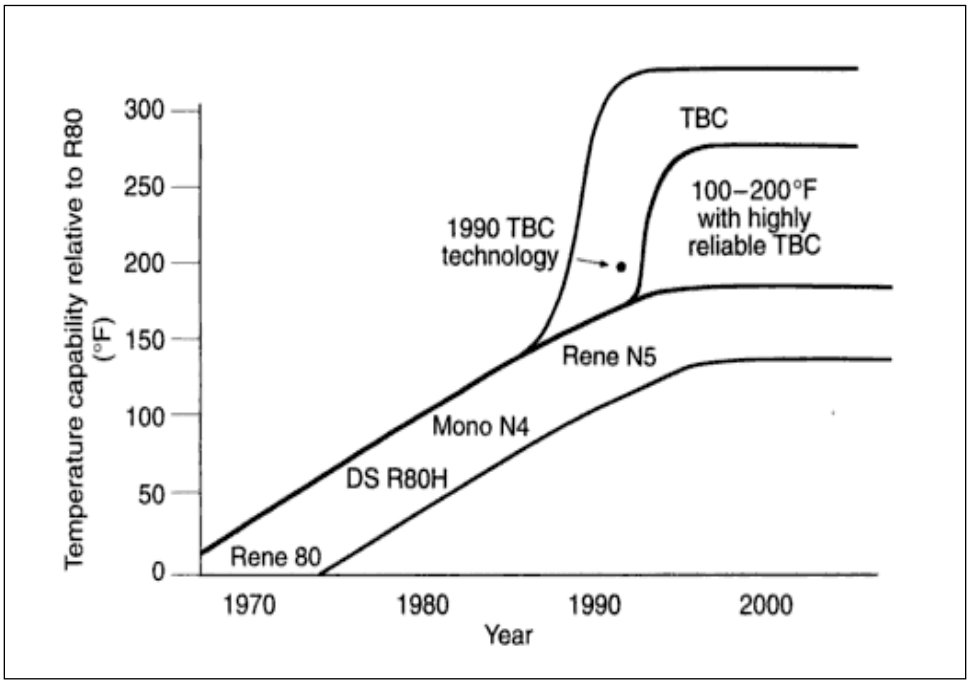

Figure 1.2: Increase in temperature capability of superalloy with time (4).

TBCs were also used in LH_2/LOX rocket engines where they extended life past one second which was a crucial development in the rocket engine program. NASA has a dedicated rocket-TBC group in Cleveland during the 90's.

1.2 TBC SYSTEM

Thermal barrier coating system is mainly made up of a base metal, a bond coat (BC), thermally grown oxide (TGO) and a ceramic top coat (TC) as shown in Figure 1.4.

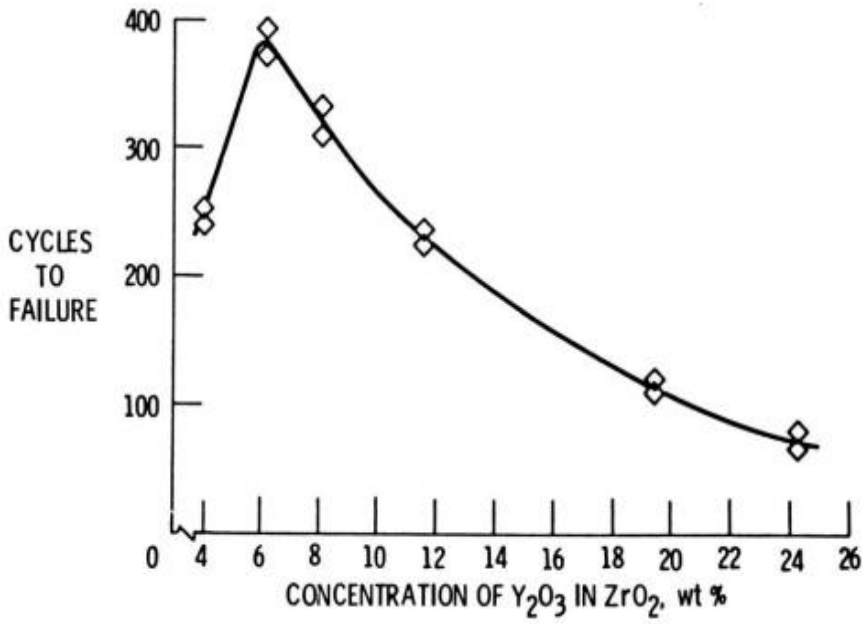

Figure 1.3: Effect of yttria composition on failure (3).

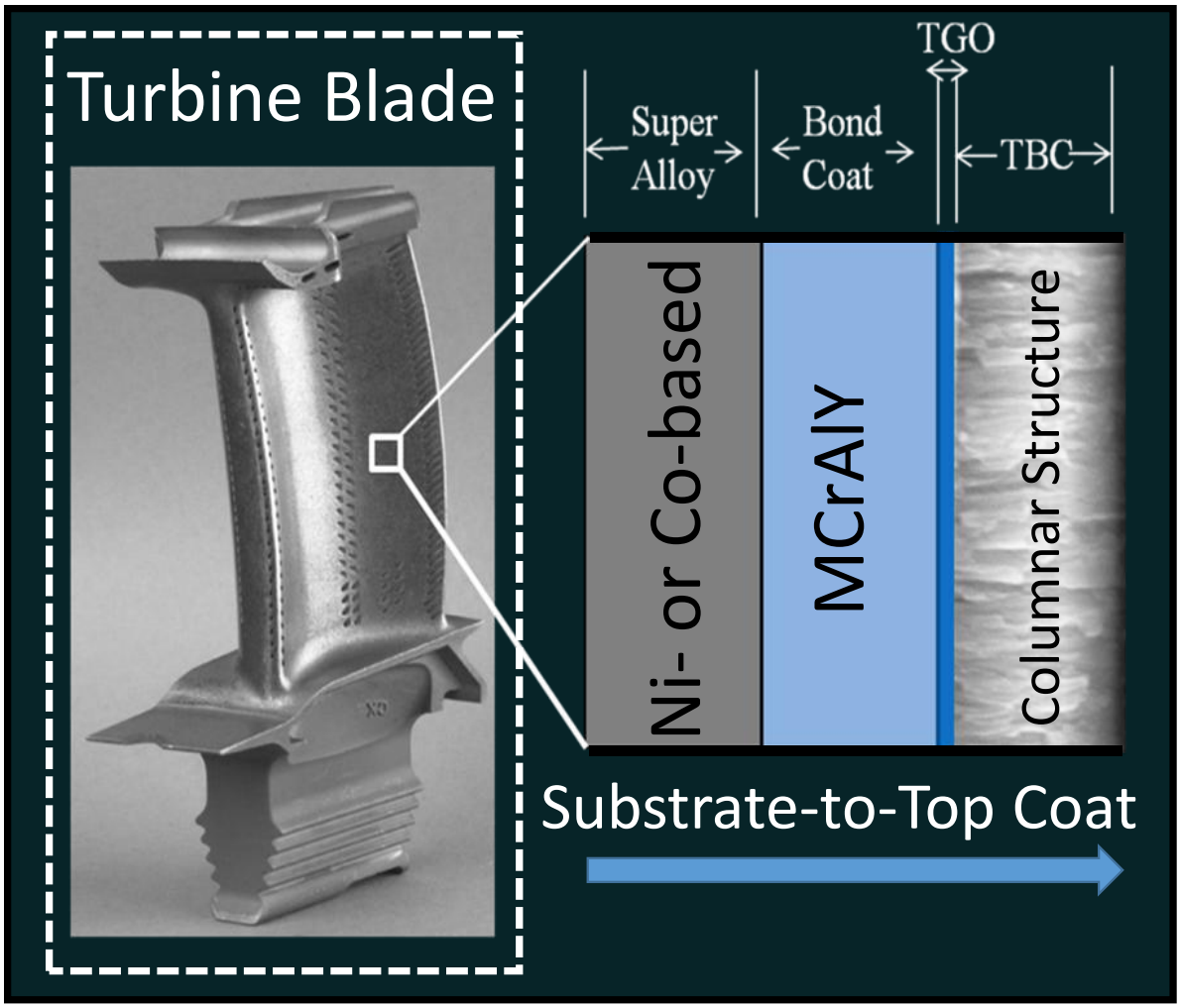

Figure 1.4: Schematic diagram of the Thermal Barrier Coatings (TBCs) system. The individual component layers are as shown in the diagram.

1.2.1 Base metal

The base metal is a Ni or Co based superalloy made from investment cast technique. This technique gives the flexibility for the design of internal cooling holes in the turbine blade that are very critical for high temperature operation. The superalloy material is made up of several different elements apart from the main elements (Ni or Co), which contribute to the high creep rupture strength, corrosion and oxidation resistance at high temperatures. The base metal

composition depends on the component it is used for. Table 1.1 shows the development of base metal compositions used for hot gas path components in the gas turbine.

Table 1.1: Base metal compositions for hot gas path turbine components (5).

Component	Cr	Ni	Co	Fe	W	Mo	Ti	Al	Cb	V	C	B	Ta
BUCKETS													
U500	18.5	BAL	18.5	-	-	4	3	3	-	-	0.07	.006	-
RENE77 (U700)	15	BAL	17	-	-	5.3	3.35	4.25	-	-	0.07	.02	-
IN738	16	BAL	8.3	0.2	2.6	1.75	3.4	3.4	0.9	-	0.1	.001	1.75
GTD111	14	BAL	9.5		3.8	1.5	4.9	3	-	-	0.1	.01	2.8
NOZZLES													
X40	25	10	BAL	1	8	-	-	-	-	-	0.5	.01	-
X45	25	10	BAL	1	8	-	-	-	-	-	0.25	.01	-
FSX414	28	10	BAL	1	7	-	-	-	-	-	0.25	.01	-
N155	21	20	20	BAL	2.5	3	-	-	-	-	0.2	-	-
GTD222	22.5	BAL	19	-	2.0	2.3	1.2	0.8	-	0.1	.008	1	-
COMBUSTORS													
SS309	23	13	-	BAL	-	-	-	-	-	-	0.1	-	-
HAST X	22	BAL	1.5	1.9	0.7	9	-	-	-	-	0.07	.005	-
N-263	20	BAL	20	0.4		6	2.1	0.4	-	-	0.06	-	-
HA-188	22	22	BAL	1.5	14.0	-	-	-	-	-	0.05	.01	-
TURBINE WHEELS													
ALLOY 718	19	BAL	-	18.5	-	3	0.9	0.5	5.1	-	0.03	-	-
ALLOY 706	16	BAL	-	37	-	-	1.8	-	2.9	-	0.03	-	-
Cr-Mo-V	1	0.5	-	BAL	-	1.25	-	-	-	0.25	0.3	-	-
A286	15	25	-	BAL	-	1.2	2	0.3	-	0.25	0.08	.006	-
M152	12	2.5	-	BAL	-	1.7	-	-	-	0.3	0.12	-	-

Turbine buckets especially stage 1 must withstand the most severe temperature and stress which makes them the limiting component in the gas turbine. Inconel 738 was used for the first stage turbine buckets from the 70's to the mid 80's before the introduction of GTD 111. These materials were cast using the investment cast technique where the molten metal solidifies from the surface towards the center of the mold, creating an equiaxed structure. Directionally solidified buckets were developed later on by exercising careful control over the temperature gradient, a planar solidification front is developed in the bucket, and the part is solidified by moving this planar front longitudinally through the entire length of the part. This resulted in an oriented grain structure that runs parallel to the major axis of the part and contains no transverse grain boundaries which adds additional creep and rupture strength (5). Currently single crystal alloy buckets are used, where the elimination of grain boundaries substantially increases the melting point of the alloy along with the creep and fatigue strength. The advantage of using single crystal alloys over equiaxed and directionally solidified alloys in low cycle fatigue is shown in Figure 1.5.

1.2.2 Bond Coat

The bond coat is a metallic layer made up of MCrAlY (where M= Ni, Co, Fe) deposited on the surface of the superalloy to improve oxidation resistance and also enhance the adherence of protective alumina. In the 90's, platinum aluminide coatings were recognized as bond coats are deposited using diffusion aluminizing technique but their application is very limited. Overlay coatings development program has been initiated by Pratt and Whitney in 1960s which led to the development of new bond coat coating compositions. In 1964 an alloy with composition Fe-25%Cr-4%Al-1%Y emerged from GE nuclear programs. A model composition of FECrAlY with

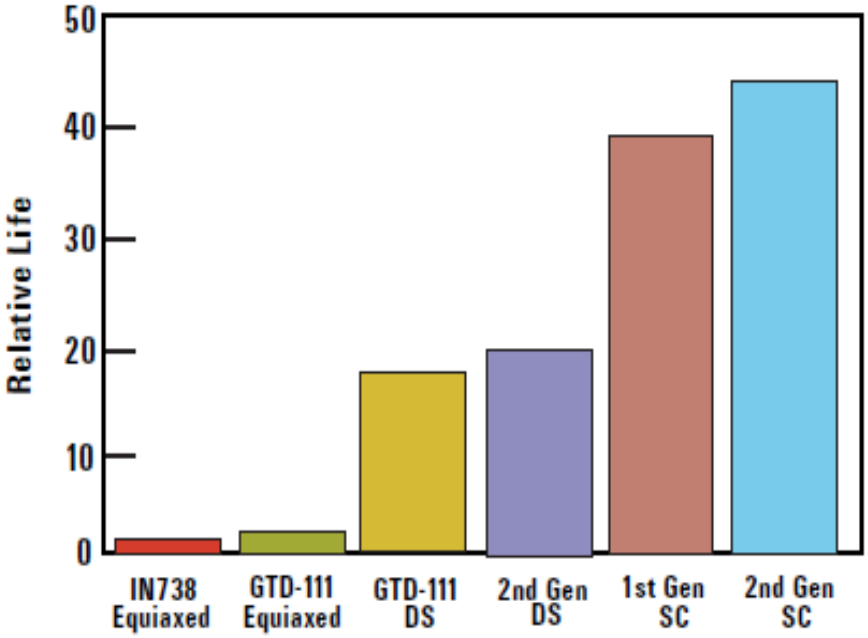

Figure 1.5: Bucket alloys-LCF life (5)

10-15% aluminum, was applied as a coating to nickel base superalloys by electron beam physical vapor deposition. The coating was not practically useful at high temperatures because nickel in the substrate alloys reacted with aluminum in the coating to form NiAl at the interface. CoCrAlY has been tried due to its high hot corrosion and oxidation resistance but, it did not meet the ductility requirements for the turbine buckets. Since NiCrAlY has limited hot corrosion resistance, a compromise was sought by adding cobalt which led to the development of NiCoCrAlY coating with a nominal composition of Ni-23%Co-15%Cr-12.5%Al-0.5%Y that had exceptional oxidation and hot corrosion properties (1). Each element present in this composition has a specific role. Ni, Co or Fe is chosen based on the superalloy material. Al is essential for the oxidation life; Cr provides hot corrosion resistance while Y is added for gettering the S which is known to segregate at the interface of the TGO and bond coat affecting the adhesion between them. Very small amounts of Si or Hf are added to promote adhesion (6).

1.2.3 Thermally Grown Oxide (TGO)

The thermally grown oxide (TGO) is a layer of alumina which grows on the surface of the bond coat during operation due to the diffusion of oxygen through the top coat material and interacts with the alumina present in the bond coat. The composition of bond coat is tailored in such a way that it acts as an aluminum reservoir for the formation of the thermally grown oxide layer. This layer prevents further oxidation and also results in discontinuities of material properties across the thickness of the coating.

1.2.4 Top Coat

The top coat (TC) is a ceramic layer which provides the required insulation to the base metal from the hot gases. The top coat material should meet certain requirements such as high melting point, low density, high thermal shock resistance, good oxidation resistance, low thermal conductivity, high coefficient of thermal expansion and resistance to particulate erosion. These material properties will be discussed elaborately in the following chapters.

1.3 Fabrication Techniques

TBCs are most commonly deposited using two different techniques; (1) air plasma spray (APS) and (2) electron beam physical vapor deposition (EBPVD).

1.3.1 Air Plasma Sprayed TBC

APS technique produces coatings with a splat microstructure (shown in Figure 1.6). These coatings have a porosity that ranges up to 25 vol% most of which occurs between the splats, which helps in reducing the thermal conductivity. The coatings produced by this method are considered cost effective from a production point of view when compared to the EBPVD deposited coatings. The mechanical durability of APS coatings is, however, very less compared to the EBPVD coatings. Hence, they are employed and suitable only in low temperature and low thermal cycling operating conditions such as those in land based gas turbines.

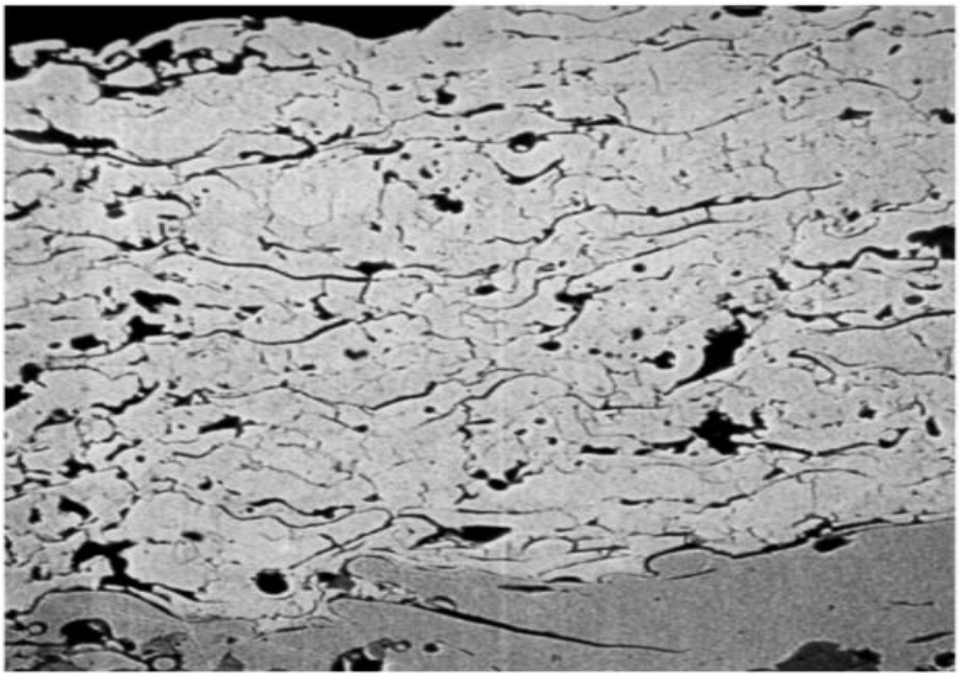

Figure 1.6: Cross Section of an Air Plasma Sprayed TBC (7).

1.3.2 EBPVD TBC

EBPVD technique produces coatings with a columnar microstructure (Figure 1.7) and smooth surface. This microstructure feature provides the necessary mechanical durability which is better than those of APS coatings. The coatings produced from this technique have improved bonding strength and the strain tolerance when compared to the APS coatings. A comparison of the properties of the APS and EBPVD properties are seen in Table 1.2.

Although EBPVD coatings have better properties to withstand in high temperature conditions, it is very expensive in contrast to APS and is only used for critical applications.

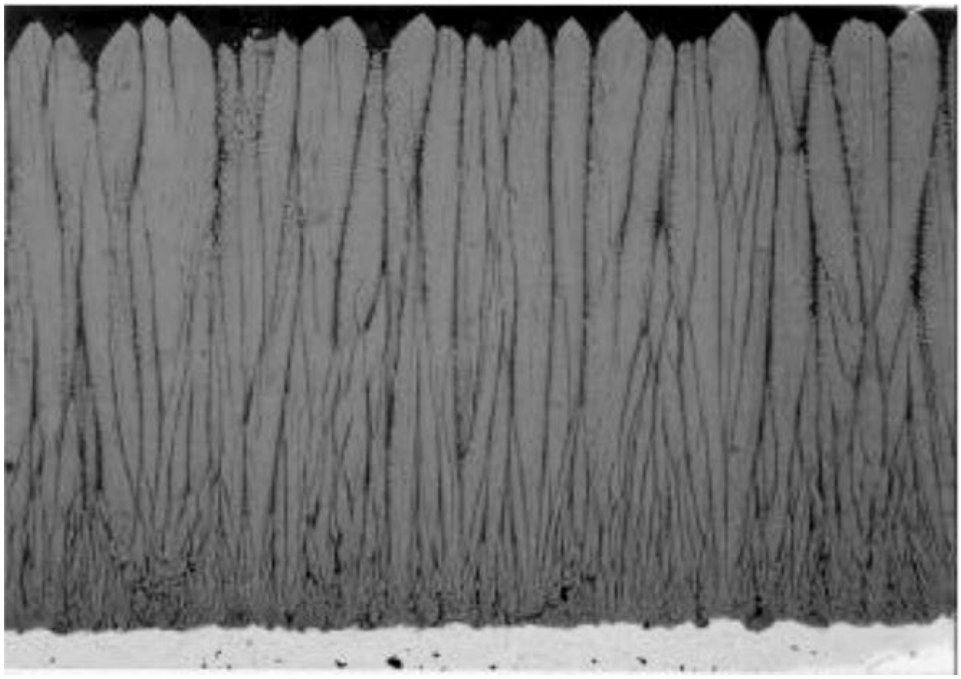

Figure 1.7: Cross section of an EBPVD TBC (7)

Table 1.2 Comparison of coating properties deposited by EB-PVD and APS (7)

Property / Characteristic	**EB-PVD**	**Air Plasma Spray**
Thermal Conductivity (W/mK)	1.5-1.9	0.8-1.0
Surface Roughness (μm)	1.0	10.0
Adhesive Strength (MPa)	400	20-40
Young's Modulus (GPa)	90	200*
Erosion rate (normalized to PVD)	1	7

1.4 APPLICATIONS

TBCs have a wide range of applications in the gas turbine. They are mainly applied to the first stage turbine buckets and nozzles along with the combustor. A typical combustor has three parts:

a fuel injection system, combustion liner and transition piece. With ever increasing demand for improved efficiency, these components are modified to withstand higher firing temperatures. This has been achieved by applying the TBCs to the combustor liners and transition pieces (as shown in Figure 1.8 and 1.9) in high temperature gas turbines.

In the present work, new ceramic top coat material properties have been investigated to understand their capability and potential to replace existing TBC top coat materials.

Figure 1.8: TBC coated combustion liner [Credit CTS]

Figure 1.9: TBC coated transition piece [Credit CTS]

Chapter 2: Literature Review

2.1 Traditional Top Coat Material

Zirconium oxide has been the traditional top coat (TC) material. The selection of this material is based on its low thermal conductivity and high thermal expansion coefficient (TEC) of the ZrO_2 cubic phase ($\alpha \sim 11\times$ 10-6 K^{-1}) in the temperature range of 20- 1200 ^{0}C. When ZrO_2 is subjected to high temperatures, its low-temperature monoclinic (M) phase transforms into the tetragonal (T) phase and then into cubic phase. Since phase transformations are involved with a change in crystal volume, it is needed to add some kind of a stabilizer to prevent phase transformations in ZrO_2. Oxides like Y_2O_3, MgO, CaO, and Yb_2O_3 are found to stabilize ZrO_2 cubic phase (8). Among those oxides, Y_2O_3 addition is found to be the most suitable for high temperature resistant coatings due to its ability to impart lower thermal conductivity by introducing point defects which is generated by the substitution of Zr^{4+} ions with two Y^{3+} ions creating an oxygen vacancy in the process (9). Considering this property, Yttria partially stabilized zirconia (YSZ) has been used for thermal barrier materials of turbine blades, bucket and combustion liner owing to its low thermal conductivity, good mechanical strength and the similarity of its thermal coefficient with that of a bond coat (10) (11).

2.2 New Top Coat Material

To improve the efficiency of the existing gas turbine systems, the operating temperatures have to be further increased. The existing zirconia based coatings undergo a phase change at temperature higher than 1200°C. This phase change from tetragonal to monoclinic is generally associated with a density change which is considered to be ~ 5 - 7.5 % (12). This change in density induces micro-cracks in the top coat and along the interface of the topcoat and bond coat, thus weakening the TBC. Ultimate result is the surface cracking, interface delaminating and final failure of the TBC. Based on this brief review and analysis, YSZ based TBCs appear to be

limited in terms of operating temperature tolerance and not a potential candidate for further improving the operating temperature.

2.2.1 Fluorite and Pyrochlore Oxides

In the search for new TBC materials, using insights from atomistic simulations and crystal chemistry, fluorite and pyrochlore structured materials were found to be the viable candidates to replace existing YSZ as a top coat material. Among the fluorite structured oxides, hafnium oxide (HfO_2) was considered to have the similar thermal conductivity as monoclinic ZrO_2. Pyrochlore structures of the form $A_2^{3+}B_2^{4+}O_7$ were found to have lower thermal conductivity than YSZ (9). Wang et.al (12) reviewed the Hafnia based ceramics. In their review, a comparison was made between zirconia and Hafnia in particular related to their phase transformation temperatures. Although HfO_2 and ZrO_2 have similar crystal structures, the tetragonal to monoclinic phase transformation temperatures were hundreds of degrees apart. The increased phase transformation temperature in HfO_2 with respect to that of ZrO_2 was explained by Grain and Campbell (13) using a metal-oxygen bond length (M-O) model. According to this model, phase transformation takes place when the M-O bond length approaches a critical value with increasing temperature. This critical temperature was said to be approximately 1050°C for Zr-O while it is around 1700°C for Hf-O. This was attributed to the fact that Zr-O bond length is larger than the Hf-O bond length which is directly related to the unit cell dimension. Another model was proposed by Gravie and Chan (14) in Wangs review which is called the partially soft lattice mechanism which explains the increased tetragonal to monoclinic phase transformation temperature in HfO_2 is based on the fact that atomic mass of hafnium (178.49) is much greater than that of zirconium (91.22). Along with higher phase transformation temperature, the melting

point of hafnia is around 2900 °C and has a low thermal conductivity of 1.5 W/mK as shown in Figure 2.1

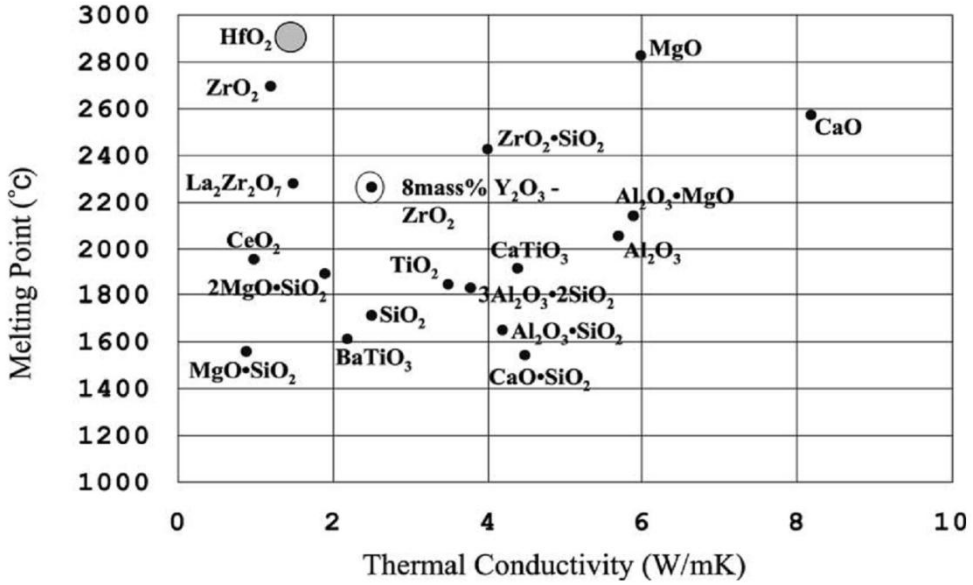

Figure 2.1: Thermal conductivity of sintered oxide ceramics (15).

2.2.2 Rare Earth Oxides

New materials that can replace the existing TBC materials need to be studied from a certain properties point of view. These properties are found to be thermal conductivity, thermal expansion, elastic modulus, hardness and thermal stability. Padture and Gell (16) performed a search for a new class of TBCs for advanced engine requirements based on these properties. Their search resulted in the identification of pyrochlore structured zirconates of the type $M_2Zr_2O_7$ (where M= Gd, Sm or Nd). The replacement of the Y^{3+} with rare earth ions is mainly to stabilize the pyrochlore structure. Powders of the three types of rare earth zirconates were prepared using the co-precipitation method, which were then hot pressed to produce fully dense ceramics. The thermal conductivities of these ceramics was found to be about 30% lower than the traditional fully dense 7 wt% Y_2O_3 stabilized ZrO_2 (7YSZ) as shown in Table 2.1. Portinha

et.al (17) produced high temperature zirconia phases at room temperature by DC reactive magnetron sputtering with a metallic Zr target doped with various quantities of Gd.

Table 2.1: Properties of different ceramics (16)

Ceramic	**Th. Conduc** $W.m^{-1}.K^{-1}$	**Th. Exp** $(°C^{-1})$	**Max. T.** **(°C)**	**El.Mod** **(GPa)**	**Hardness** **(GPa)**	**Density** $(g.cm^{-3})$
Target	<2.0	$>10\times10^{-6}$	>1600	<250	>6	<7
7YSZ	2.3	10×10^{-6}	1425	200	14	6.4
$Gd_2Zr_2O_7$	1.6	11.6×10^{-6}	2300	205	10	7.0
$Nd_2Zr_2O_7$	1.6	-	2300	-	10	6.4
$Sm_2Zr_2O_7$	1.6	10.8×10^{-6}	2400	231	11	6.7

Rare earth oxides were considered as stabilizers in place of the alloying oxides. This was based on the fact that high mass additions which will provide more phonon scattering centers (18). Nicholls *et.al* (7) studied the thermal conductivities of various dopant additions and found that Gadolinia has the lowest thermal conductivity as shown in Figure 2.2.

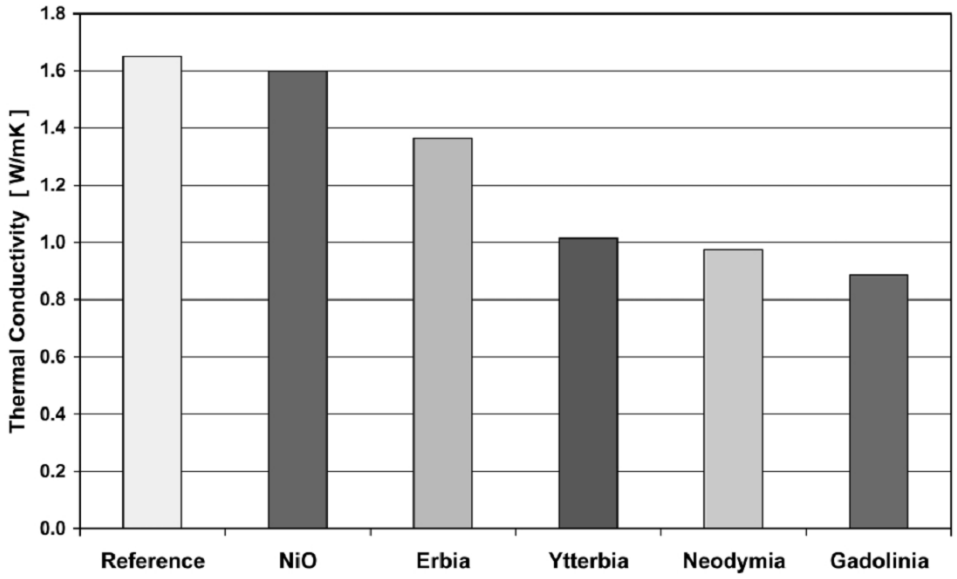

Figure 2.2: Thermal conductivity of rare earth oxides (7)

Maloney (19) in his work showed that the thermal conductivity of Gd_2O_3-HfO_2 thermal barrier coatings is very less than that of the current YSZ based TBCs. Chandan et.al (20) studied the effect of Gd_2O_3 content on the crystal structure and phase of the HfO_2 ceramics. When the concentration of Gd_2O_3 was varied from 0 to 12 mol%, the Gd_2O_3-HfO_2 ceramic system exhibited monoclinic to a mixture of monoclinic and fluorite structure. At 20 mol% of Gd_2O_3, only fluorite phase was found. The formation of single phase pyrochlore $Gd_2Hf_2O_7$ phase formation occurred with increasing Gd_2O_3 concentration to 38 mol%.

Apart from the improvement in thermal conductivity, rare earth oxides have been proven to increase the cyclic oxidation resistance. Ramanathan et.al (21) has investigated the effect of rare earth oxide coatings on the oxidation resistance of chromia forming alloys. In their work, sols of La_2O_3, CeO_2, Pr_2O_3, Nd_2O_3, Sm_2O_3, Gd_2O_3, Dy_2O_3, Y_2O_3, Er_2O_3 and Yb_2O_3 were prepared and sprayed on the alloys to form a coat. The uncoated and coated specimens were subjected to cyclic oxidation tests, and was found that the RE oxide coated specimens withstood higher number of cycles that the uncoated specimens. Also, among the RE oxide coatings, only specific coatings could withstand more than 15 cycles as shown in Table 2.2. This increase in oxidation resistance of the rare earth oxides has been attributed to the RE ionic radius. The RE ions diffuse through the oxide scale to the gas interface after prolonged oxidation through the grain boundaries. Due to its larger ionic radius, it inhibits the outward diffusion of alloy cations through the grain boundaries preventing further oxidation. As shown in Table 2.2 La_2O_3, Pr_2O_3 and Gd_2O_3 could withstand higher number of cycles due to their higher ionic radius when compared to the other oxides. This concept of higher ionic radius can also be applied to the TBC coatings, where a RE oxide addition can reduce the interaction of oxygen with the bond coat thus prolonging the time taken to form oxide layer or reducing its thickness between the top coat and

bond coat interface along with increasing the life of the TBC. Based on the concept of increased oxidation resistance and thermal conductivity as discussed earlier, Gd_2O_3 has been chosen as the material of choice for doping the hafnia coatings.

Table 2.2: Cycles to rare earth oxide spallation (21)

Oxide	**Number of Cycles at spall**
Lanthanum	15+
Cerium	9
Praseodymium	15+
Neodymium	12
Samarium	12
Gadolinium	15+
Dysprosium	6
Yttrium	7
Erbium	7
Ytterbium	4

2.3 EROSION

Erosion of TBC is one of the important failure mechanisms to be considered. This mechanism is more predominant in the EBPVD coatings which have a columnar microstructure. Effects of variables such as the type of erodent (either silica or alumina), velocity of the erodent and the impact angle have been studied (22). Wellman *et.al* (23) has classified the damage mechanism due to erosion in EBPVD TBCs into three modes.

Mode I (near surface cracking): In this mechanism, the damage is confined to the top 20-30μm of the surface of the individual columns. Material is lost only when a large number of columns have been impacted and cracked.

Mode II (Compaction damage): This is a damage mechanism, intermediate between small particles erosion and FOD and may act as the transition between these two mechanisms, where there is compaction of the EB PVD TBC columns but neither the near surface cracking of Mode I nor the gross plastic deformation, kinking and cracking of Mode III (FOD) is observed. Column compaction, but not fracture occurs, resulting from the surface impact and is attributed to the high porosity levels in the columns and the lower stain rates associated with the impact. The columns of these coatings are less than 90% dense. A similar type of compaction occurs during Mode I, where the damage is limited to the near surface region of one or two columns and lateral cracks then initiate from the elastic/plastic interface. However, when the impact is spread over a significant number of columns, as is Mode II compaction damage, cracks do not initiate at this interface. This is thought to be due to a lower rate of energy input by the decelerating particle, resulting in a lower strain rate.

Mode III Foreign object damage (FOD): FOD is caused by large particles travelling at low velocities and intermediate velocities or smaller particles at higher velocities and is characterized by significant deformation of the coating which can penetrate to the substrate and is accompanied by gross plastic deformation of the columns. The FOD is further classified into two types. FOD type 1 is the mechanism of gross plastic deformation of the coating with the associated densification bending and cracking of the columns. FOD type 2 involves significant buckling of adjacent columns and plastic deformation without any significant degree of cracking.

The different modes of damage discussed are not purely dependent on impact velocity and particle size but rather the relative size of the contact footprint to the column diameter and the strain rates that result during the period of contact.

Studies have also been performed on the effect of ageing and dopant addition on the erosion mechanisms of TBC. Wellman and Nicholls (24) have studied different aged heat treated samples with the aim of sintering the ceramic columns. They found that the heat treatments resulted in a significant increase in the erosion rates when compared to the as-received samples. For the samples given the higher temperature heat treatment, the increase in the erosion rate was attributed to the fact that the columns were partially sintering together which enabled cracks to propagate into neighbouring columns, as opposed to stopping at column boundaries as occurs in samples that have not been heat treated. Steenbaker et.al (25) have studied the effects of dopants on the erosion resistance of EB PVD TBCs by studying the effects of 2 mol% Gd_2O_3 additions on the room and high temperature erosion resistance of as received and aged EB PVD TBCs. They performed the test on samples heat treated to 1100˚C for 100 hrs and 1500˚C for 24 hours. At higher ageing temperature for the standard TBC there is evidence of columns sintering together, the boundaries between individual columns is less defined and the pyramidal top is smoothed. On the contrary the doped TBC shows no evidence of sintering and the top of the columns are still pyramidal hence it is difficult to distinguish the sample that has been aged from the as-received sample. Sintering is evident in the cross-section micrograph of the doped TBC aged 24 hours at 1500°C however it appears that sintering is less pronounced than in the standard TBC. It has been proposed that dopant additions introduce immobile defect clusters reducing the movement of atoms hence increasing the sintering resistance of the coating (25). On the one hand improvement in sintering resistance due to gadolinia addition means that the columns of

doped TBCs should be less sintered and therefore it should be more difficult for the cracks to propagate to the neighboring columns and this would result in a lower material loss hence a better erosion resistance.

2.4 THERMAL CONDUCTIVITY

Thermal conductivity of the TBCs is measured by several techniques. But only a select few have been adopted. Almeida (26) and Huang (27) have used the laser flash technique to measure the thermal conductivity of the TBCs. The principle of this method involves heating on one side of the specimen using a laser pulse and measuring the temperature rise on the opposite side. The time required for the heat to travel from one side to the other is used to calculate the diffusivity α which in turn is used to calculate the thermal conductivity using the relation

$$K = \alpha c_p \rho \quad \ldots\ldots\ldots\ldots\ldots (1)$$

Wolfe (28) used the steady state laser heat flux approach to measure the thermal conductivity of EB-PVD 8YSZ thermal barrier coatings. Zheng (29) used time domain thermoreflectance method at a single delay time to measure the depth profile of thermal conductivity for heat flow along both the through-thickness and the in-plane directions of an EBPVD YSZ coating. 3ω method developed by Cahill (30) and photo-acoustic method (31) are other methods that can be used to measure the thermal conductivity of TBCs.

Nicholls *et.al* (7) have identified four significant factors that may lower the coating thermal conductivity by modifying either phonon and/or photon transport.

(1) The introduction of atomic level defects, such defects include atoms of different mass, vacancies and interstitials and can be introduced by adding dopant, or by ion bombardment. These defects are effective in reducing phonon conduction (heat transfer by lattice vibrations).

(2) Coloring of the thermal barrier coatings can be used to increase the coatings opaqueness to

infra-red radiation. This is achieved through the addition of dopant materials and reduces the radiative transport through the coating.

(3) Nano-grained structures act to scatter both phonons and photons. The fine, micro-crystallite zone observed within the nucleation region of EB-PVD thermal barrier coatings behaves in this way. Renucleation of the EB-PVD coating growth at periodicities less than 100μm would lower the ceramic coatings thermal conductivity.

(4) Layering involves the introduction of interfaces/density changes parallel to the ceramic bond coat interface. These layered structures are effective in reducing both radiative and phonon transport.

2.5 NON DESTRUCTIVE EVALUATION

The degradation of the thermal barrier coatings can be studied using various nondestructive techniques, one of which is Impedance Spectroscopy (IS). This method is used for evaluation of defects and degradation of materials by using the AC frequency response of the electrical impedance of a material. Ogawa et.al (32) evaluated the formation kinetics and physical properties of the reaction layer formed in the TBC during operation by Impedance Spectroscopy. They observed that specimen aged at higher temperature and longer duration showed larger impedance. They also learned that the impedance behavior of the TBC was found to change remarkably by the formation of the reaction layer. Zhang Dan Hua et.al (33) investigated the oxidation behavior in co-doped zirconia coatings using IS.

2.6 FABRICATION PROCESS

Singh and Wolfe (34) made a comparison of the various processes that can be used to fabricate the TBC coatings. The details are as shown in Table 2.3.

Table 2.3: Comparison of fabrication process (34)

Coating Process	**Substrate temp.(C)**	**Deposition rate**	**Surface roughness**	**Type of bonding**	**Typical microstructure**	**Coating Material**	**Environment**	**Flexibility**
Plasma spray	RT to 800 (flexible)	>100µm/min	Very rough	Mechanical	Deformed lamella	Metal, Ceramic	Noise	Flexible
CVD	>800-1200 (must)	<0.08µm/min (<5µm/h)	Smooth	Diffusional	Columnar, Equiaxed	Metal, Ceramic	Chemical gas disposal	Limited
PVD-Sputtering	<600 (flexible)	<0.08µm/min (<5µm/h)	Smooth	Diffusional	Columnar	Metal, Ceramic	Clean	Limited
EB-PVD	RT to 1200 (flexible)	0.01 to 100µm/min	Smooth	Diffusional	Columnar, Nanograined equiaxed	Metal, Ceramic	Clean	Flexible

Chapter 3: Research Objectives

3.1 Problem Statement

Gas turbines are being pushed to operate at higher firing temperatures to improve their efficiency and reduce emissions. Existing thermal barrier coatings based on zirconia have a limit on their operational temperature and cannot meet the growing demand for operational efficiency. Hence, there is a need to develop new ceramic materials that can replace the existing YSZ top coat materials. The goal of the current work is to develop thermal barrier coatings that can withstand higher operating temperatures using electron beam physical vapor deposition (EBPVD) technique and test them for gas turbine applications.

3.2 Significance

Due to recent changes in the energy policy and concern over global warming, there is a pressure on engineers to increase the efficiency of the engines that utilize fossil fuels for power generation. One way of increasing the efficiency is to increase the operating temperature which helps in burning fuel more efficiently.

Hafnium oxide based coatings have the capability to replace zirconia coatings due to their higher phase transformation temperature. The addition of rare earth oxides into the hafnia system further reduces the thermal conductivity of the TBC. Thus, successful fabrication of these gadolinia doped hafnia coatings can lead to higher firing temperatures contributing to improved efficiency of gas turbines. Thus, the overall work plan (Figure 3.1) is to fabricate and characterize GSH coatings and to derive a structure-property relationship.

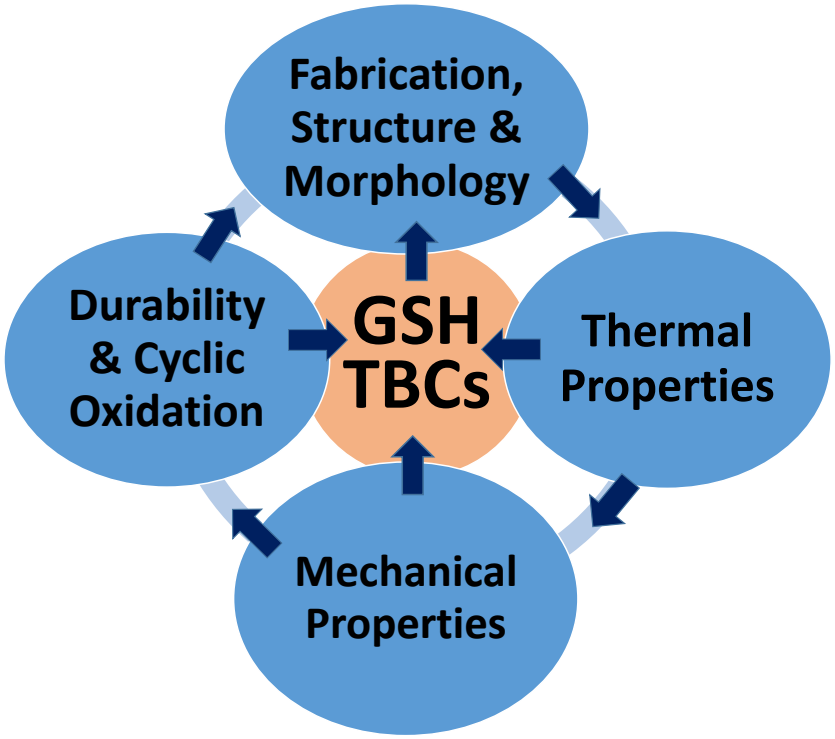

Figure 3.1: Overall work plan

3.3 OBJECTIVES

1. Prepare various compositions of Gd_2O_3-HfO_2 ranging from 4-38mol% Gd_2O_3.
2. Fabricate HfO_2 coatings doped with Gd_2O_3 using EBPVD technique on Inconel -738 substrates deposited with NiCoCrAlY bond coat.
3. Characterize the as deposited coatings using SEM, XRD and nanoindentation techniques to understand the structural, morphological and mechanical properties.
4. Expose the coatings to high temperature cycling to test their durability and cyclic oxidation.
5. Measure the specific heat and thermal diffusivity of the bulk compositions and the fabricated coatings.

Chapter 4: Experimental Techniques

4.1 Coating Fabrication

The different constituent layers of materials needed to fabricate the TBC system were deposited using either Air Plasma Spray (APS) or Electron Beam Physical Vapor Deposition technique (EBPVD). The top coat ceramics were primarily produced by the EBPVD method.

4.1.1 Air Plasma Spray (APS)

This technique uses electrically generated plasma to heat and melt the feedstock material that is fed into spray gun in the form of a wire or powder. The temperature of the plasma is on the order of 10,000˚C where the feedstock melts rapidly and is propelled towards the substrate. A stream of molten and semi-molten particles impinges on the surface and forms a coating. When the particles hit the substrate they mechanically lock onto the surface, deform and cool rapidly. The bonding of the particles is through mechanical interlocking or through diffusion. High velocity of particles leads to better bonding and higher density of the coating. In the present work, APS has been used for the deposition of the bond coat on Inconel-738 substrates. A schematic of the operation of a plasma spray is shown in Figure 4.1. The parameters used for the bond coat deposition are recorded in Table 4.1

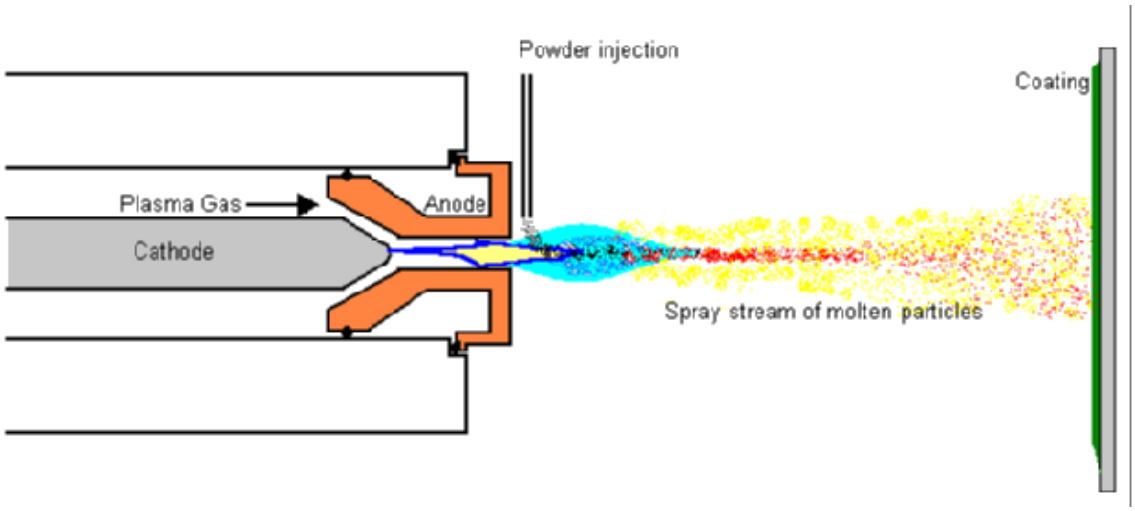

Figure 4.1: Plasma spray process

Table 4.1: Parameters used for bond coat fabrication

Parameters	
Material	CoNiCrAlY
Gun System	Metco 3MB
Nozzle	GH
Air cap/Jet	Uni-jet 3M 275
Primary gas	Argon
Pressure	98 – 105 psi
Flow	75 - 85
Secondary gas	Hydrogen
Pressure	45 – 55 psi
Flow	15 - 25
Carrier gas	Argon

Pressure	-
Flow	35 - 40 psi
Amps	480 - 520
Volts	60 - 70
Spray rate	7 - 7.5 lb.hr
Spray distance	4 - 5 inches

4.1.2 Electron Beam Physical Vapor Deposition (EBPVD)

This technique uses an electron beam to vaporize a ceramic ingot placed in a water cooled copper crucible. A typical EBPVD system consists of an electron beam gun and an evaporation unit that contains the material to be evaporated. The electron beam gun consists of an electron emitter (filament) which emits a beam of high energy electrons. The power of the electron beam depends on the accelerating voltage and the beam current given to the gun. A permanent magnetic field deflects and focuses the beam through a 270 degree arc (as shown in Figure 4.2) where the beam impacts the target material present in the crucible. The kinetic energy of the impinging electrons is transformed into thermal energy at the impact surface (target material). Since the bottom of the crucible is water cooled, the heating process takes place only on the surface allowing a consistent vapor emitting zone. The vaporized material condenses on to the surface of the substrate present above the evaporator and forms a coating which is usually columnar in structure.

The setup used for the present work is as shown in Figure 4.3. An e-vap 4000 Electron Beam Evaporation Source as shown in Figure 4.4 is used. The evaporation unit is a 4 pocket 30cc water cooled copper crucible. A 10 KV power supply is used to provide the required

accelerating voltage. The vacuum chamber is equipped with a cryo-pump to generate the necessary vacuum required for the deposition process. A sweep controller is provided to achieve a uniform evaporation of the material which is done by moving the beam over the surface of the material by varying the current supplied to the electro-magnetic coils. The chamber is evacuated to a pressure of 10^{-6} torr. The voltage is maintained at 8.18 KV (this value varies based on the type of evaporator used) and the beam current is varied to achieve the required power necessary to evaporate the material. The thickness of the coatings is monitored using a quartz crystal oscillator positioned next to the sample platform.

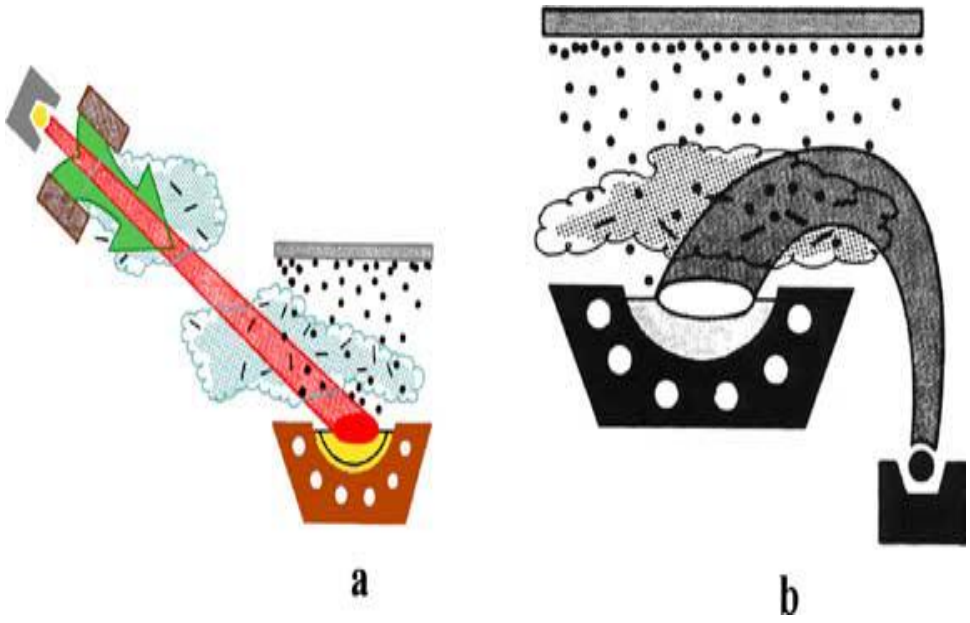

Figure 4.2: a) Undeflected and b) deflected e-beam (34)

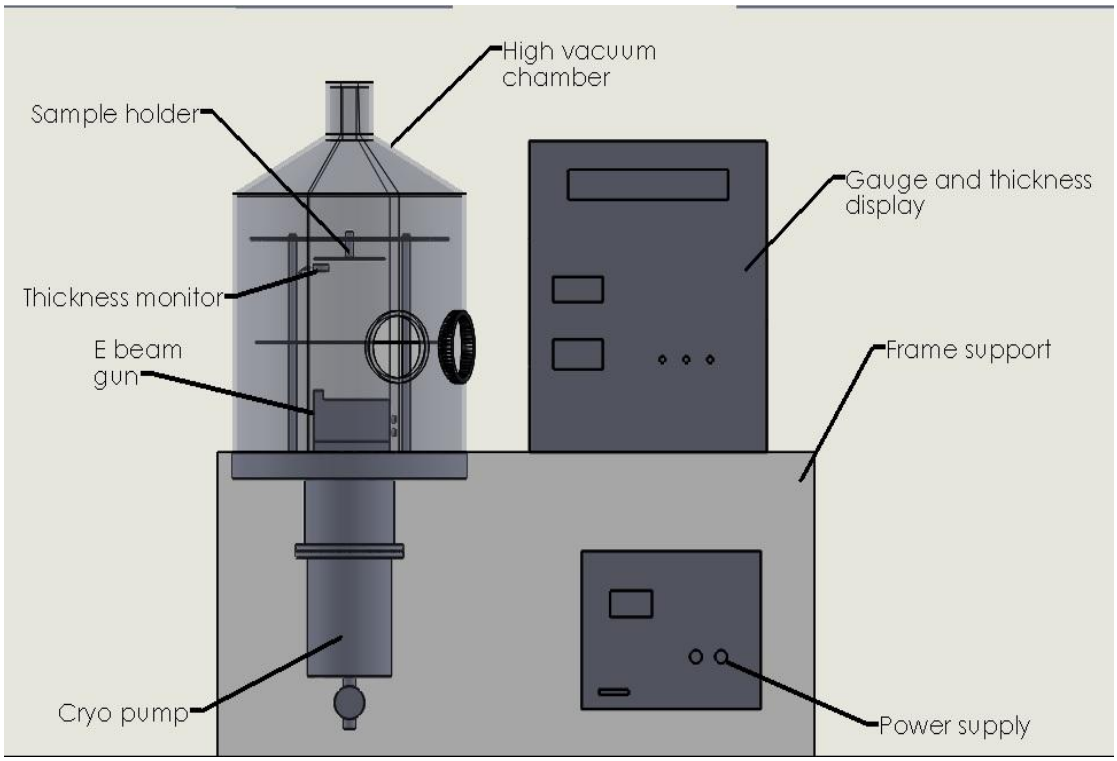

Figure 4.3: Schematic of the EB-PVD setup

Figure 4.4: Evap 4000 evaporation source

Table 4.2: Deposition Parameters

Material	**Substrate**	**Base pressure (torr)**	**Deposition pressure (torr)**	**Voltage (KV)**	**Current (mA)**	**Temperature (˚C)**
HfO_2	Inconel-738 Sapphire	10^{-6}	10^{-5}	8.18	220	27
4mol% Gd_2O_3 – 96mol% HfO_2 (GSH 4-96)	Inconel-738 Sapphire	10^{-6}	10^{-5}	8.18	220	27
12mol% Gd_2O_3 – 88mol% HfO_2 (GSH 12-88)	Inconel-738 Sapphire	10^{-6}	10^{-5}	8.18	220	27

4.2 MATERIALS

In the current work, different coating compositions were used for evaporation onto various substrates of Inconel-738 and sapphire. The compositions along with the substrates and the deposition conditions are as shown in Table 4.2. The specimens at various stages of the deposition are shown in Figure 4.5.

Bulk materials of the specified compositions were also prepared in the form of pellets. The appropriate ratio of Gd_2O_3 and HfO_2 were grinded and mixed together in a mortar. PVA (Polyvinyl Alcohol) was added to the mixture as a binder. The mixed compositions were transferred into an 8 mm diameter die and compressed at high pressures using a hydraulic compressor. After compression, the pellets were sintered in a furnace at 1400˚C for 24 hours with a heating and cooling rate of 10˚C/min.

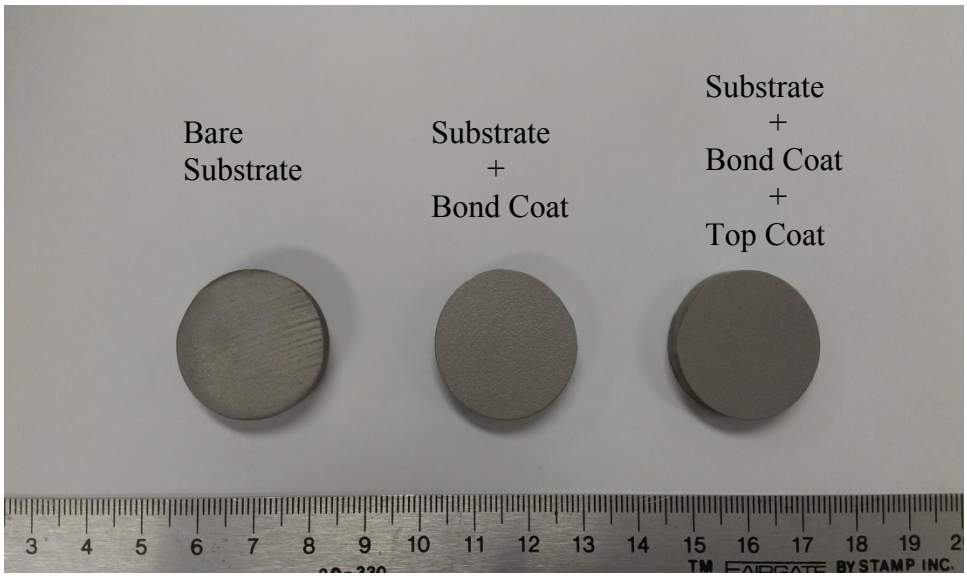

Figure 4.5: Inconel 738 samples

4.3 METALLOGRAPHIC PREPARATION

The samples were prepared by metallographic technique to study the interface between the coating and the substrate. Small, squared samples were mounted using an epoxy resin so that, the coating is provided with edge protection during polishing.

The grinding/polishing process was performed in eight different steps using a metallographic table. The first seven steps involved using silicon carbide abrasive disks while the last step involved using a velvet napped cloth. Samples were first subjected to planar grinded using a 180 grit SiC paper for about 60 sec. The next steps involved fine grinding using a 240, 320, 400, 600, 800 and 1200 grit SiC paper for about 25 sec each. The final polishing step was performed using a 1µm diamond paste on a velvet napped cloth for about 30 sec. The samples were cleaned and dried after every grinding /polishing step before moving into the next step.

4.4 MATERIAL CHARACTERIZATION

4.4.1 Surface morphology and interface analysis

The coatings' surface morphology and interface structure was characterized using a Hitachi S4800 Scanning Electron Microscope (SEM) shown in Figure 4.6. The grain size and surface morphology of the as deposited coatings were obtained using secondary electron imaging. Cross sectional imaging analysis was also performed on the samples to obtain information on the coating-substrate interface and the coating thickness.

Figure 4.6: Hitachi S-4800 Scanning Electron Microscope

4.4.2 Structural analysis

A Bruker D8 Advance X-ray diffractometer (XRD) shown in Figure 4.7 has been used for the structural characterization. XRD is an analytical technique in which x-ray beam hits the surface of a substrate at various incident angles scattering preferentially oriented x-rays into

detector which collects them to generate crystallographic information about the sample such as lattice parameter, d-spacing, film orientation. XRD principle is based on Bragg's law:

$$\lambda = 2d\sin\theta \quad \ldots\ldots\ldots\ldots\ldots\ldots\ldots\ldots\ldots\ldots\ldots \text{(2)}$$

Where,

λ = wave length of X-ray, d = inter planar distance and θ = Bragg's angle.

The as deposited coatings were characterized to investigate the crystal structure and phase obtained from the XRD patterns.

Figure 4.7: Bruker D8 Advance XRD

4.4.3 Mechanical properties and tribology

The mechanical properties of the coatings were determined by performing nanoindentation using Nano Test Vantage equipment by Micro Materials at temperatures up to 750° C which is helpful in determining the hardness and modulus of elasticity of the TBC coatings under high temperature conditions. This instrument uses electromagnetic force

application to indent the samples and capacitive depth measurement to continuously measure the indentation depth. The depth of penetration was decided based on the thickness of the sample (usually 1/10 of the sample thickness). The load was applied on the sample using the indenter till the maximum penetration depth was reached. The indenter was held at this maximum depth and then removed. The load applied at the maximum depth is the maximum load applied on the sample. The indentation curves (loading and unloading) obtained from this method are used to calculate the hardness and modulus of elasticity of the coatings as defined by Oliver and Pharr (35). A schematic of the indentation curves is shown in Figure 4.8.

Hardness (H), is defined by the maximum load divided by the area of the indentation.

$$H = \frac{W_{max}}{A} \quad \text{..... (3)}$$

The reduced modulus of elasticity of the coatings is determined from the slope of the unloading curve (dw/dh) called stiffness, S (1/compliance) (at maximum load) (36).

$$\frac{1}{S} = \frac{1}{2E_r}\sqrt{\frac{\Pi}{A}} \quad \text{..... (4)}$$

Where,

A= area of the indentation at the contact depth

E_r= reduced modulus of elasticity

The elastic modulus is related to the reduced modulus of elasticity E_r as,

$$\frac{1}{E_r} = \frac{(1-\nu_i^2)}{E_i} + \frac{(1-\nu_s^2)}{E_s} \quad \text{..... (5)}$$

Where, Ei and νi are related to the diamond indenter tip which is equal to 1140 GPa and 0.07.

Fatigue fracture testing was performed on the coatings using nano-impact capability within the Nano Test Vantage developed by Micro Materials. The testing was achieved by

repetitive impacts with cube corner diamond indenter accelerated rapidly over a precisely chosen distance to impact the surface at very high strain rates.

Figure 4.8: Nano Test Vantage Equipment [Credit: Micro Materials UK]

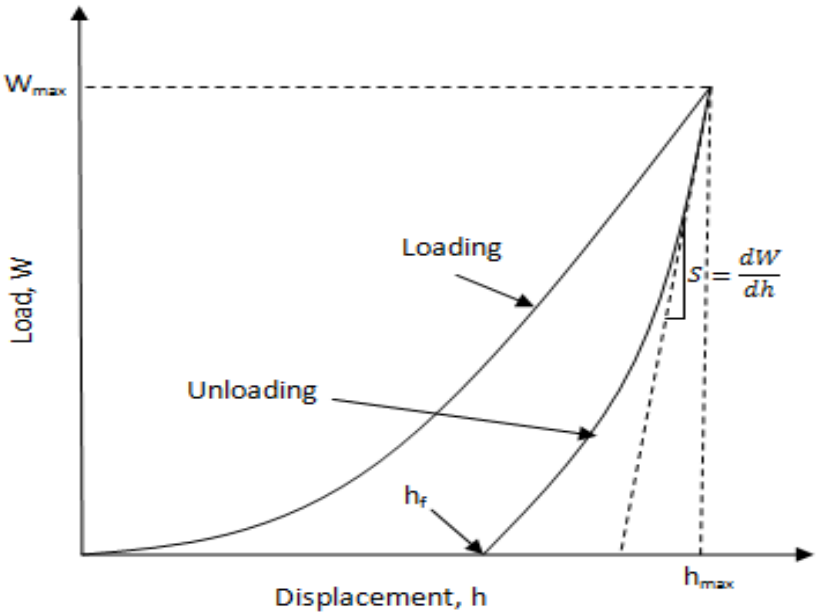

Figure 4.9: Load-displacement curve

4.4.4 Thermal conductivity

The thermal properties of the coatings were determined using Differential Scanning Calorimetry (DSC) and Laser Flash technique. The DSC technique was used (Figure 4.10) to determine the specific heat of the different coating compositions. In this technique the difference in the amount of heat required to increase the temperature of a sample and its reference (with a defined specific heat) is measured as a function of temperature. The heating stage for both the sample and the reference is incremented at the same rate to avoid any discrepancies in measurements.

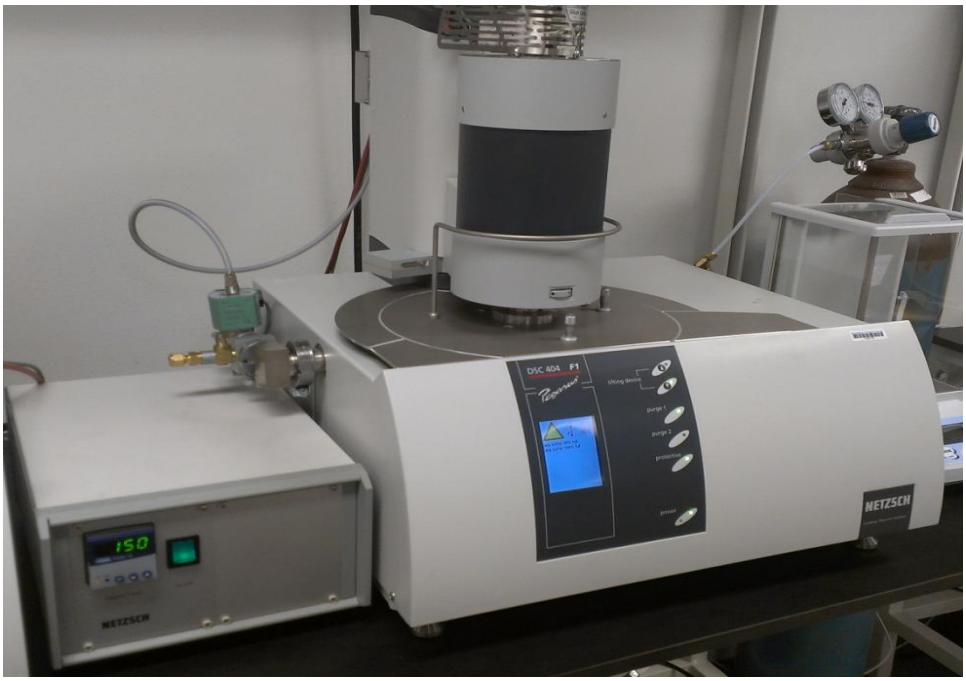

Figure 4.10: NETZSCH DSC

A Netzsch LFA 457 Laser flash instrument (Figure 4.11) was used to determine the thermal diffusivity of the coatings used to calculate the thermal conductivity of the coatings. In this technique, the front face of the coating is homogeneously heated by an unfocused laser pulse. On the rear face of the specimen the temperature increase is measured as a function of

time. The mathematical analysis of this function allows the determination of the thermal diffusivity ‘a’.

For adiabatic conditions, thermal diffusivity is determined by the equation

$$a = 0.1388\frac{l^2}{t_{0.5}} \text{..... (6)}$$

Where

a = thermal diffusivity in cm^2/s

l = thickness of the specimen in cm

$t_{0.5}$ = time at 50% of the temperature increase measured at the rear end of the specimen in seconds.

Figure 4.11: Netzsch LFA 457

4.4.5 Thermal Cycling

The samples were subjected to thermal cycling using a CM high temperature cycling furnace (Figure 4.12). The temperature was set to 900˚C with a cycle time of 60 minutes, which includes 10 minute ramp up, 40 minute dwell and 10 minute cool down. The surface morphology and crystal structure information of the coatings were gathering before the exposure. Samples were subjected to one cycle initially and studied for changes in surface morphology and crystal structure. Then the number of cycles was increased to 10, 25, 50, 100 and 200 while studying the samples after the end of each of these sets.

Figure 4.12: High temperature thermal cycling furnace

4.4.6 Thermal Oxidation

The samples were subjected to thermal oxidation at a temperature of 900˚C at first for a time period of 5 hours. The weight of the samples before and after exposure to high temperature

was measured using a very sensitive weight balance. Once the measurements were taken, the sample was exposed to the same temperature again for another 5 hours and weight measurements were noted. After this step, the exposure time was increased to 10 hours and 20 hours for one increment each, and then 30 hours till a total exposure time of 160 hours was reached.

4.4.7 Impedance Spectroscopy

Impedance Spectroscopy measurements were performed on the bulk material pellets using an LCR meter. Impedance spectra can be interpreted to characterize the electrical properties of the materials and relate the changes in these electrical properties to microstructural changes occurring in the materials (33). The thermal cycled pellets were polished with silver paste on both sides of their surface and heated in a furnace at 90˚C for two hours. The pellets were then sandwiched between two thin silver foils and then connected by silver wires to HP (4284A) precision LCR meter (Figure 4.13). The assembly constitutes the parallel plate capacitor geometry with the different composition pellets as the dielectric. An ac signal of 1V and frequency (f) in the range of 20Hz – 1 MHz was applied to the circuit using HP precision LCR meter.

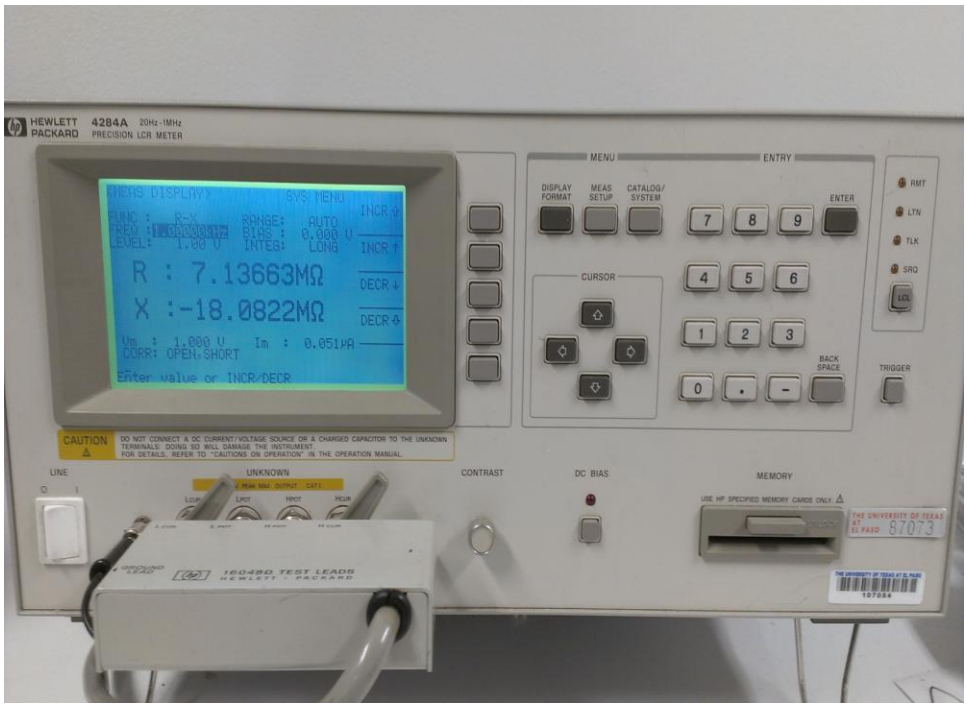

Figure 4.13: HP (4284A) Precision LCR meter

Chapter 5: Simulation

A finite element model was developed to study and compare the stresses and mechanics of degradation of Yttria stabilized Hafnia (YSH) and YSZ (Yttria stabilized Zirconia) top coat as a result of thermally grown oxide growth. This model resolves the strain energy partitioning between the top, base and bond coats. A temperature dependent J2 plasticity law is employed along with inclusion of temperature dependent thermal expansion, growth and damage.

5.1 MODELING

A two-dimensional three layer system (Figure 5.1) consisting of the top coat, thermally grown oxide (TGO) and bond coat was modeled in ABAQUS. The ceramic layer was treated as an elastic material, while the thermally grown oxide and the bond coat were considered as elastic-plastic materials. The materials characteristic parameters and data used in the model are as presented in Tables 5.1 - 5.5. The model was meshed in Altair Hypermesh using ABAQUS 4 node continuum plane stress elements (CPS4R). The mesh was very refined at the free edge while gradually becoming coarse as moves away towards the constrained edge. The initial size of the TGO was set to one micron. Its growth has been simulated using a time-dependent volumetric expansion model called SWELLING available in ABAQUS, by which its thickness reaches three microns by the end of the cycling process. A J2 plasticity law with a user defined isotropic strain hardening curve has been used in the model.

Swelling behavior is expressed as:

$$\dot{\mathcal{E}}^{sw}=(r_{11}+\ r_{22}+r_{33})\frac{1}{3}\dot{\mathcal{E}} \quad \text{..... (7)}$$

where $\dot{\mathcal{E}}$ is the volumetric strain rate and $r_{11}, r_{22} and\ r_{33}$define the material growth direction. Since, we are considering the growth of the TGO layer only in the Z direction which is perpendicular to the interfaces, r_{11} and r_{22} are equal to zero.

$$\dot{\mathcal{E}}^{sw} = r_{33}\frac{1}{3}\dot{\mathcal{E}} \ldots\ldots\ldots\ldots\ldots\ldots \quad (8)$$

The thermal stresses developed in this model can be defined using the equation:

$$\sigma(T) = \frac{E(T)}{(1-\nu^2)}\alpha(\mathrm{T})\Delta\mathrm{T} \ldots\ldots\ldots\ldots \quad (9)$$

where σ (T) is the thermal stress, α(T) is the thermal expansion coefficient at temperature T, ΔT is the temperature gradient, E(T) is the elastic modulus and ν is the poisons ratio.

5.1.1 THERMAL CONDITIONS

Each cycle (Figure 5.2) in the thermal cycling process has three steps. The first is a heating step where the temperature is ramped from room temperature to 1200 ˚C in 5 min. In the second step, the temperature was held at 1200 ˚C for a duration of 10 min. The third step is a cooling phase where the temperature is dropped from 1200 ˚C to room temperature in 5min. The system is set to run for 75 cycles during the thermal cycling process. The node sets have been defined at the top coat, between the interfaces and the bond coat. Each node set was given a specific temperature which was controlled during the cycling process using the amplitude option. The temperature gradient across the system was kept at 400 ˚C. The base, bond coat, TGO and top coat are modeled explicitly

Table 5.1: Material data for YSZ (37)

Temperature (˚C)	α (K^{-1})	E (GPa)	ν
20	9.68E-6	17.5E3	0.2
400	9.7E-6	-	0.2
700	9.88E-6	-	0.2
900	-	12.4E3	0.2
1000	1.034E-5		0.2

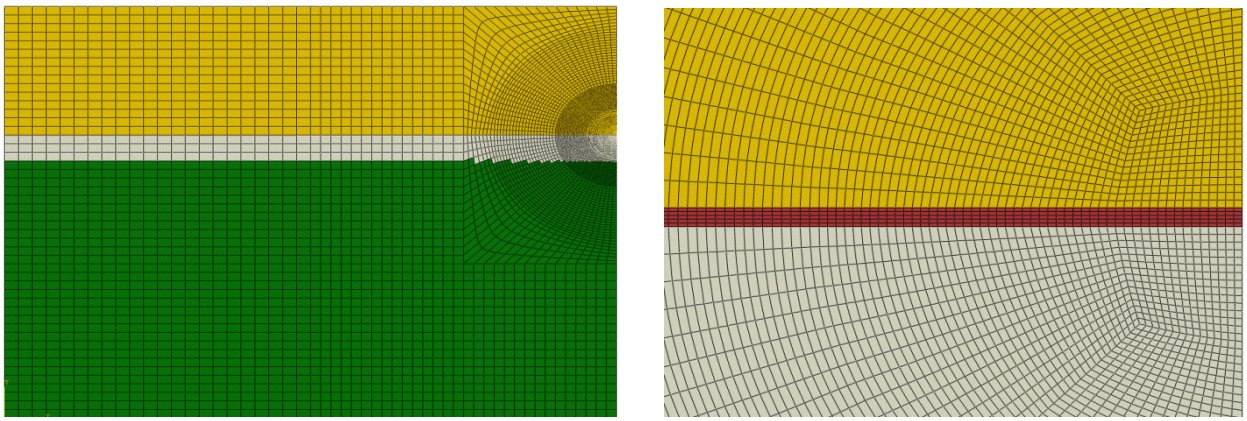

Figure 5.1: Finite element mesh employed showing refinement at the peel region of the interface.

Table 5.2: Material data for TGO (38)

Temperature (˚C)	$\alpha(K^{-1})$	E (GPa)	ν
25	5.1E-6	380E3	0.27
600	-	353E3	0.27
800	-	338E3	0.27
1000	-	312E3	0.27
1165	9.8E-6	-	0.27

Table 5.3: Material data for YSH (39)

E (GPa)	240E3
ν	0.25
$\alpha(K^{-1})$	9.2E-6

Table 5.4: Plastic data for BC (40)

Temperature (˚C)	Stress (MPa)	Plastic Strain
25	1000	0
400	2500	0.23
600	2200	0.3
800	375	0.022
900	60	0.02
1000	19	0.01

Table 5.5: Material data for BC (38)

Temperature (˚C)	$\alpha(K^{-1})$	E (GPa)	ν	A ($h\ MPa^{n})^{-1}$	n	M
20	-	183E3	0.3	-	-	-
100	1.034E-5	-	0.3	-	-	-
200	1.13E-5	-	0.3	6.4E-10	1.8	-0.19
400	1.25E-5	152E3	0.3	-	-	-
500	-	-	0.3	2.2E-9	1.9	-0.21
600	-	-	0.3	-	-	-
700	-	-	0.3	-	-	-
800	1.43E-5	55E3	0.3	-	-	-
850	-	-	0.3	-	-	-
900	1.6E-5	-	0.3	9.7E-7	3.4	-0.31
1000	-	-	0.3	-	-	-

5.1.2 DAMAGE MODEL

A damage evolution model was used to study the degradation of the material. This model assumes that the damage is characterized by the progressive degradation of the material stiffness matrix leading to the material failure and is used in conjunction with the damage initiation criteria. This criterion is a model (41) used for predicting the onset of damage due to nucleation, growth and coalescence of voids. The model assumes that the equivalent plastic strain at the onset of damage$\mathcal{E}_D^{pl}$ is a function of stress triaxiality and strain rate:

$$\mathcal{E}_D^{pl}(\eta, \dot{\mathcal{E}}^{pl}),$$

where η=-p/q is the stress triaxiality, p is the pressure stress, q is the Mises equivalent stress and $\dot{\mathcal{E}}^{pl}$ is the equivalent plastic strain rate. The criterion for damage initiation is met when the following condition is satisfied:

$$\omega_D = \int \frac{d\mathcal{E}_D^{pl}}{\mathcal{E}_D^{pl}(\eta, \dot{\mathcal{E}}^{pl})} = 1 \text{..... (10)}$$

where $\omega_D$is a state variable that increases with plastic deformation.

The degradation of the material stiffness matrix is written as:

$$\sigma = (1 - D)\bar{\sigma} \text{ ..... (11)}$$

where D is the damage variable. The stress-strain behavior of a material undergoing damage is as shown in Figure 5.3. In the figure, σ_y and $\mathcal{E}_i^{pl}$ are the yield stress and the equivalent plastic strain at the onset of damage, i.e., when D=0 and $\mathcal{E}_f^{pl}$ is the equivalent plastic strain at failure when the overall damage variable reaches D=1.

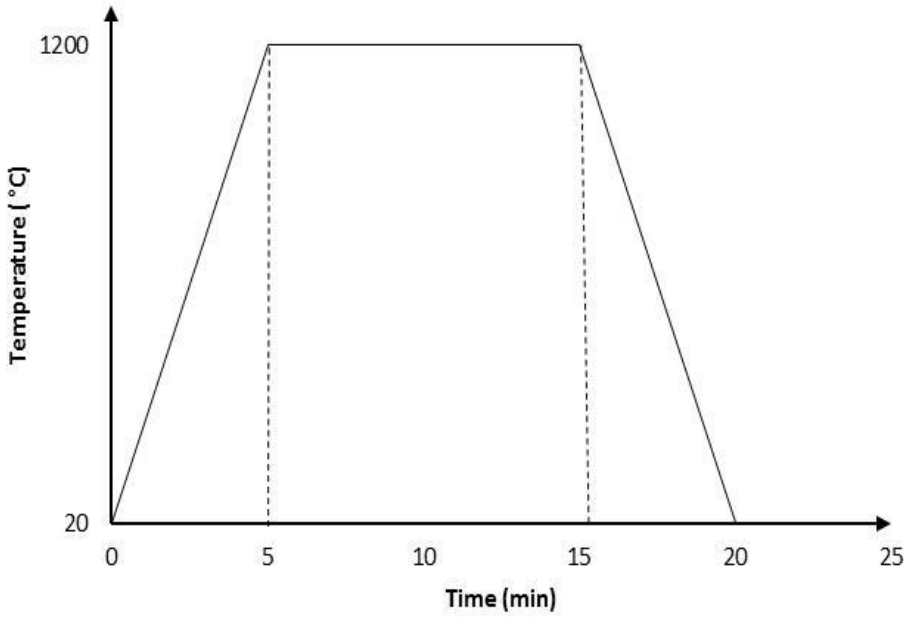

Figure 5.2: Thermal Cycle

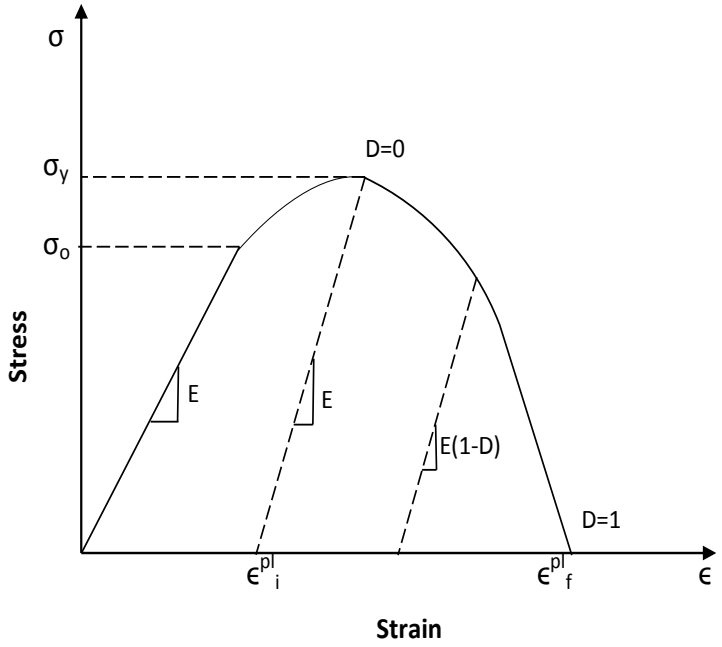

Figure 5.3: Stress-strain curve of material undergoing damage

Chapter 6: Results and Discussion

6.1 Crystal Structure

The crystal structure of the GSH coatings deposited on Inconel 738 substrates was studied using XRD. The XRD patterns obtained are shown in Figure 6.1, where the peaks are as indexed. It can be noted that the (111) peak corresponds to the gadolinia monoclinic phase while the (200) peak relates to the hafnia cubic phase. This observation indicates the stabilization of the high temperature cubic hafnia phase at room temperature by the addition of gadolinia. With an increase in gadolinia content, it can be noticed that the peaks shift by an angle of 0.43˚ towards the lower diffraction angles. This indicates the change of the crystal structure to the fluorite phase which further changes into pyrochlore phase with an increase in gadolinia which is consistent with the results reported by Chandan et al (42). From the XRD pattern, it can be noticed that the peaks are rather broad indicating the presence of nano particles. This was confirmed by fitting the (111) peak using a Gaussian distribution which gives the value of the FWHM (full width half maxima) of 0.646 which was used for calculating the crystallite size of using the Scherrer equation.

$$d = \frac{\eta\lambda}{\beta cos\theta} \quad \ldots\ldots\ldots\ldots\ldots \quad (12)$$

where,

d = crystallite size

η= shape factor, 0.9

λ= X-ray wavelength (1.54 Å for Cu)

β= Full width half maximum (FWHM)

θ= Bragg's angle

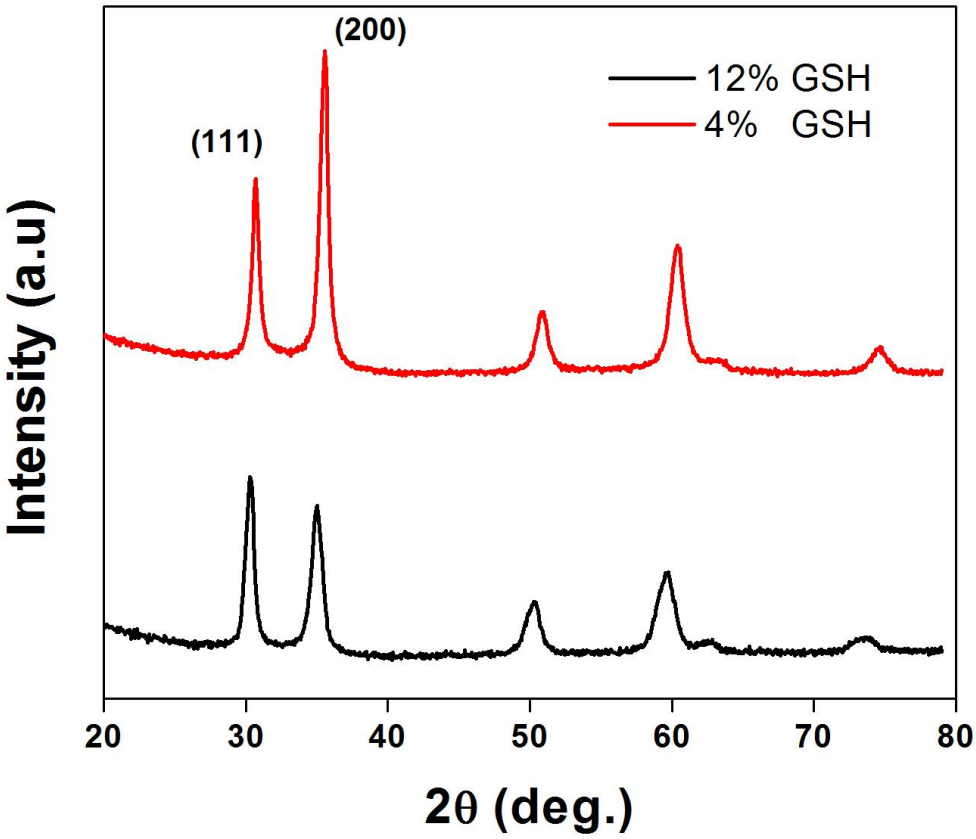

Figure 6.1: XRD patterns for as deposited coatings

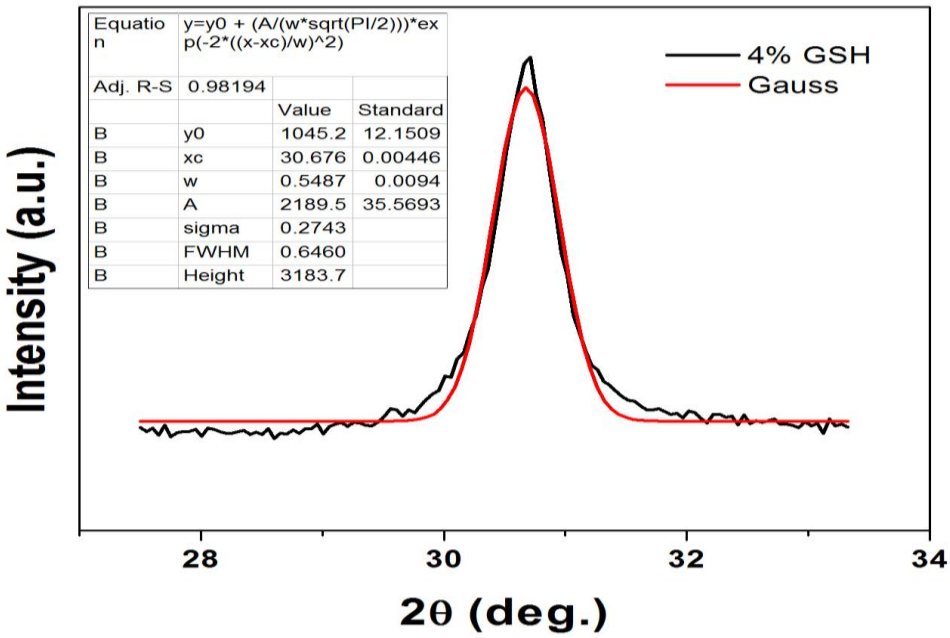

Figure 6.2: Gaussian fit

6.2 SURFACE MORPHOLOGY

The surface morphology of the GSH coatings has been studied using scanning electron microscopy (SEM). For comparison, the GSH coatings and as deposited bond coats without the top GSH coatings were examined. The surface of the as deposited bond coat material on the Inconel substrates is as shown in Figure 6.3. As can be seen from the SEM image, the surface of the bond coat has a very high surface roughness due to the inherent nature of the deposition process. However, it should be noted that the bond coat surface roughness can contribute to the failure and delamination of the TBCs. Therefore, the bond coat surfaces were subject to sand blasting prior to deposition of the top coat to reduce the roughness. The surface of the coatings after deposition of the top coat material are as shown in Figures 6.4 and 6.5. The morphology of the coatings is very smooth which is representative of the presence of Gadolina.

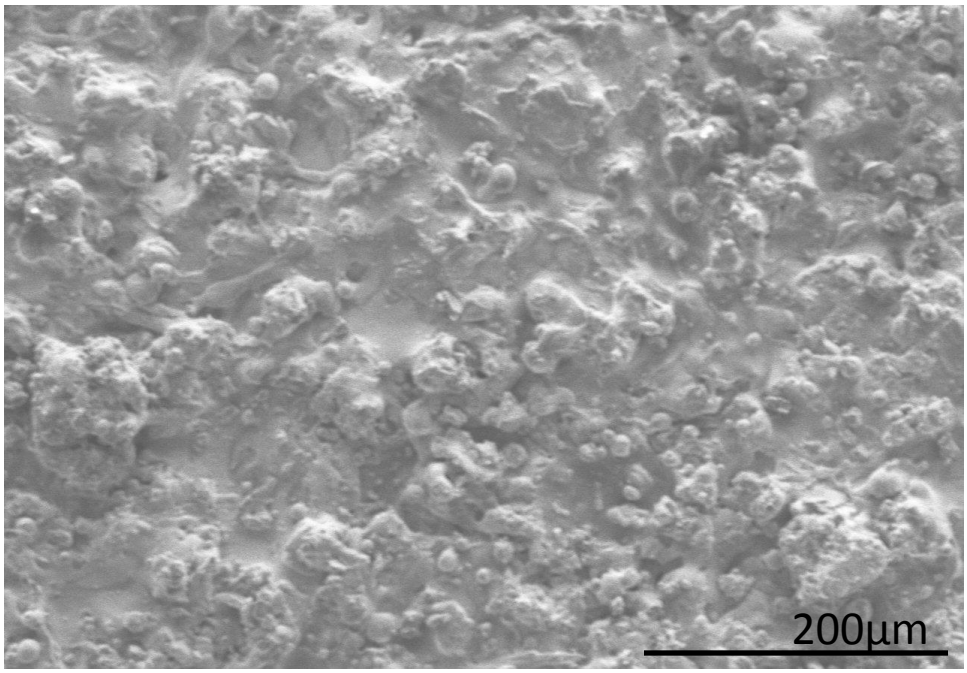

Figure 6.3: Bond Coat

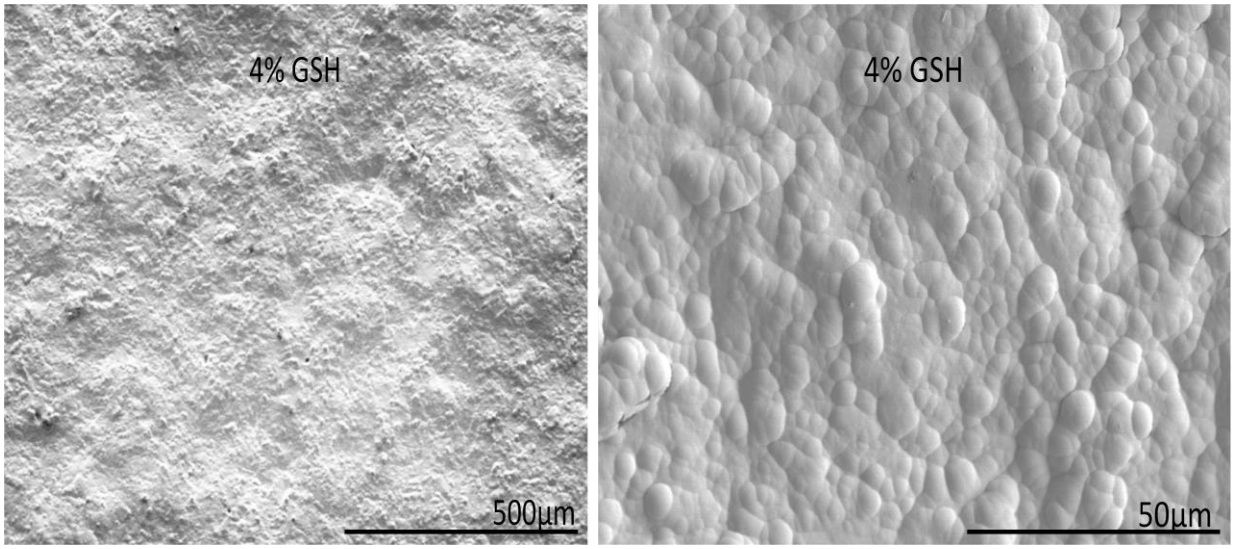

Figure 6.4: Surface morphology of 4 mol% GSH

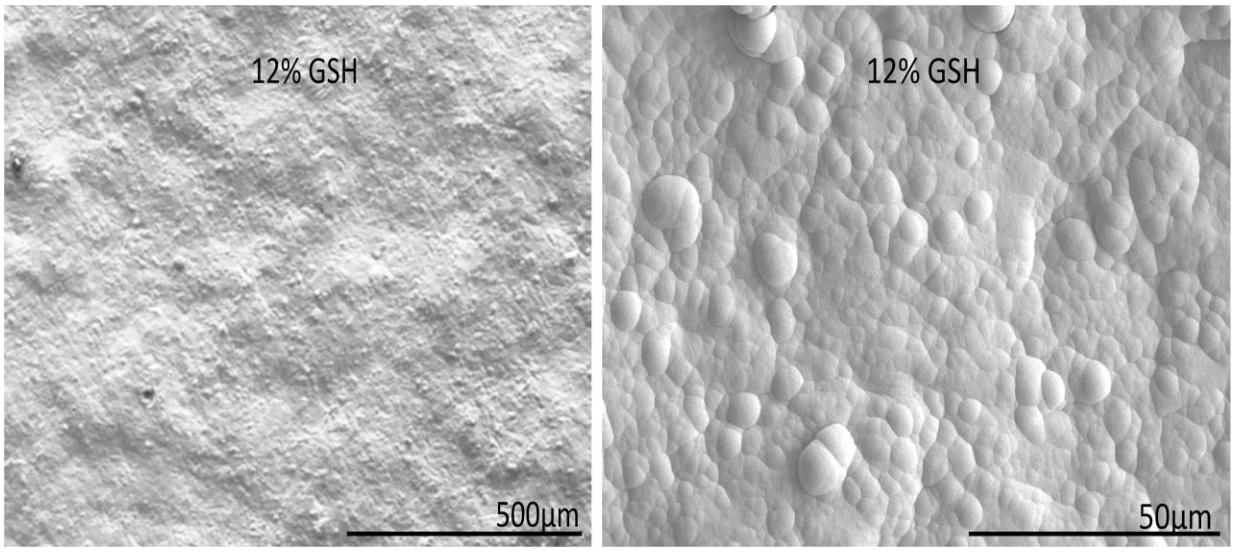

Figure 6.5: Surface morphology of 12 mol% GSH

6.3 CROSS SECTION – INTERFACE MORPHOLOGY

The coated samples were sectioned and mounted in a resin and metallurgical polishing was performed as mentioned earlier. The cross section of the samples was studied using the SEM. The top coat, bond coat and the substrate are as shown in Figure 6.6. The thickness of the coatings was ~15 microns. This was consistent with the reading obtained from the quartz crystal monitor used to monitor the coating thickness during the deposition process. The cross section of the coating deposited exhibits columnar structure (Figure 6.7) which is a signature of EBPVD deposited coatings. This columnar structure is very important since it imparts mechanical durability to the TBC (43). The thickness of the columns is found to be less than 1 µm. The significance of this characteristic feature will be discussed further when the mechanical properties of the coatings are considered later below. The sharp interface between the top coat and bond coat material seen in the Figure 6.6 indicates that there is no reaction between these two layers. No segregation or diffusion of the layers present. Also, there is no visible separation between the two layers indicating a good adhesion between them.

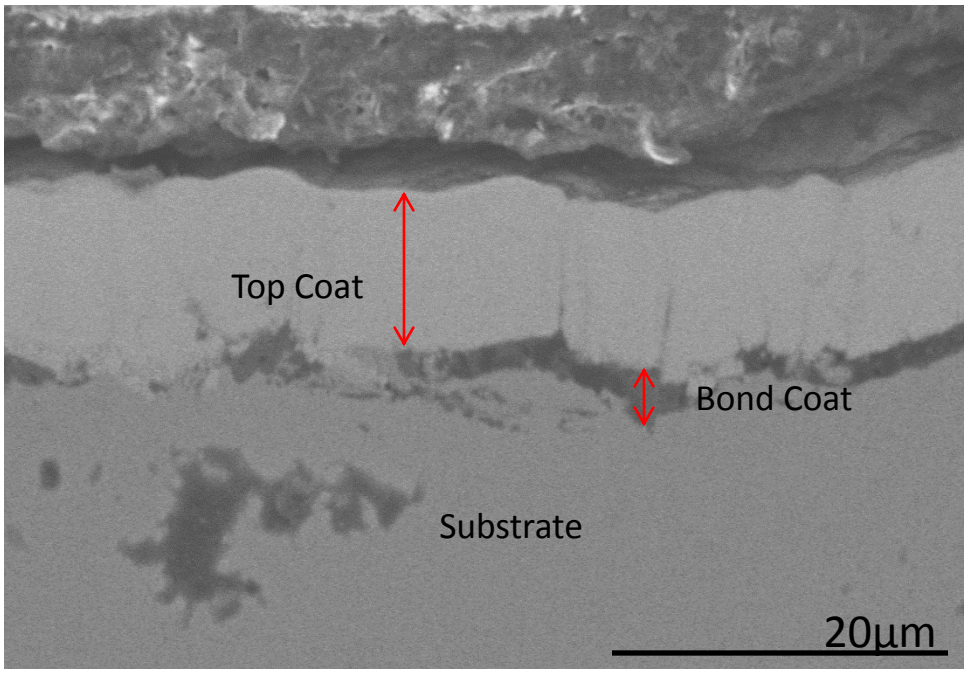

Figure 6.6: Cross section of TBC on Inconel substrate

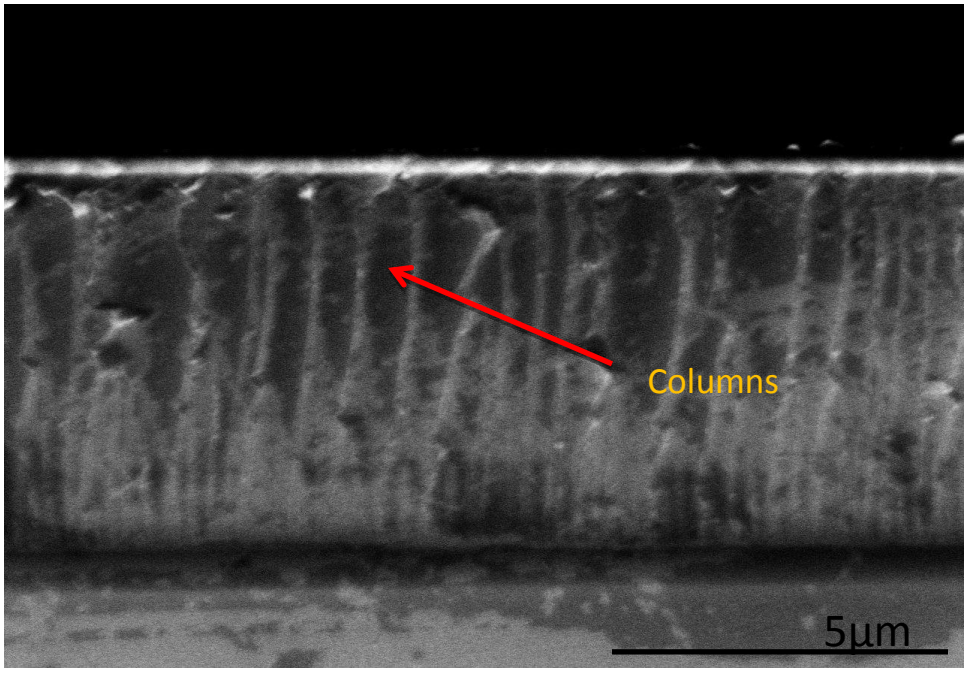

Figure 6.7: Cross Section showing the columnar structure

6.4 MECHANICAL PROPERTIES

Nanoindentation has been performed on pure and Gd_2O_3 incorporated hafnia coatings. The measurements were performed on 0-12 mol% Gd_2O_3 doped HfO_2 and some selected samples of 4 mol% GSH coatings. The load-displacement characteristic curves of these samples are as shown in Figure 6.8 and 6.9. It can be noticed that, the curves of the as deposited samples with an increase in the gadolinia content in hafnia tend to shift towards the right. The hardness (H) and reduced modulus (Er) were calculated from these load-displacement curves using the Oliver and Pharr method (35). It can be noted that the hardness and stiffness values decrease with increasing of gadolinia content in the ceramics (Figure 6.10 and 6.11). This may be attributed to the fact that the increase of alloying oxide content in hafnia reduces its hardness (44). On the other hand, the hardness and stiffness values of the 4mol% GSH coatings increased after heat treatment at 900˚C for 15 hours shown in figure 6.12 and 6.13. This could be due to the sintering effect.

High temperature nanoindentation has also been performed on 4 mol% GSH coatings. The testing was performed at a temperature of 750 ˚C to study the hardness and elasticity profile of the material. Figures 6.14 and 6.15 presents a comparison between the hardness and elasticity values obtained both at room temperature and high temperature nanoindentation. It can be noticed that the hardness value decreases with increasing temperature. This behavior in the TBCs was previously observed in the work done by Kim et. al (45), where the reduction could be due to the softening of the material which allows the indenter to further penetrate into the surface.

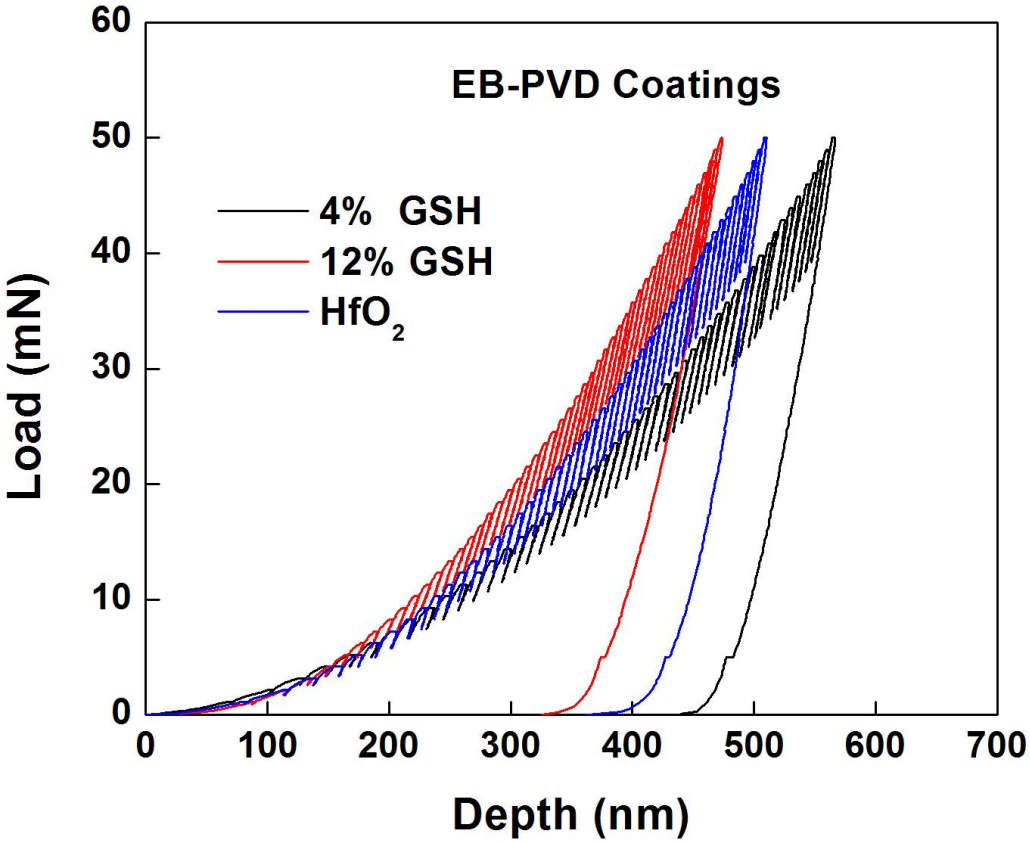

Figure 6.8: Load-displacement curves for varying gadolinia content

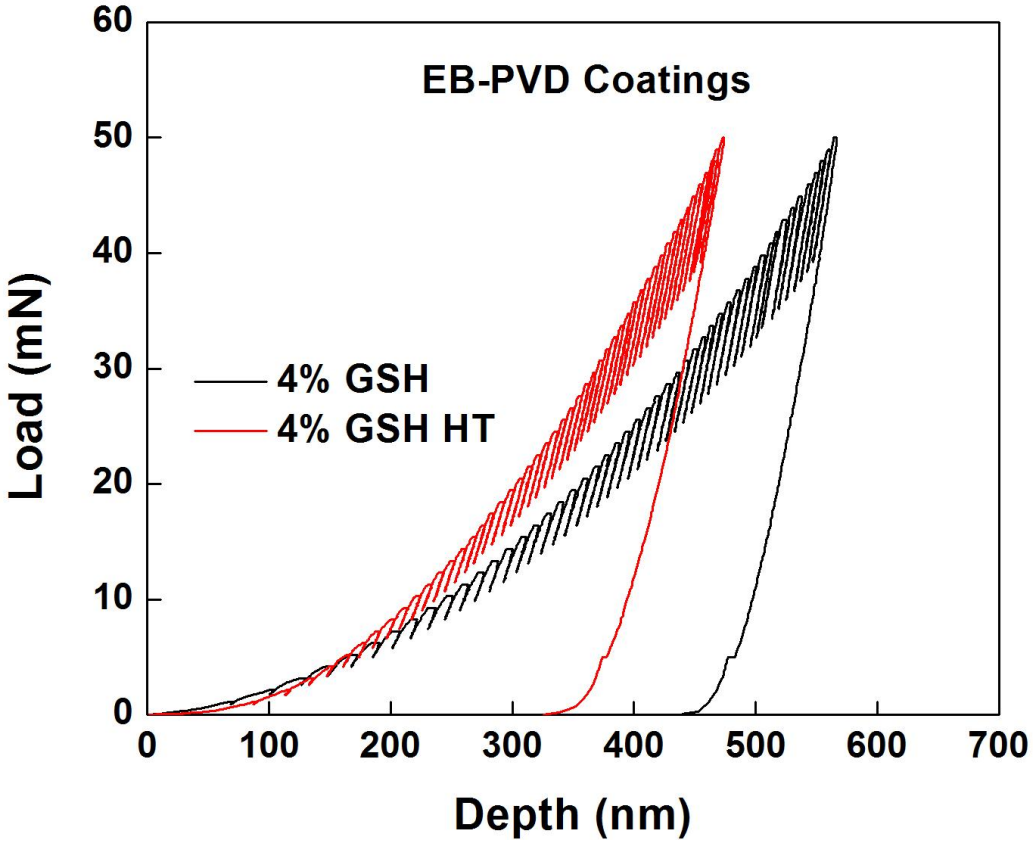

Figure 6.9: Load displacement curve for as deposited and heat treated 4mol% gadolinia doped coatings

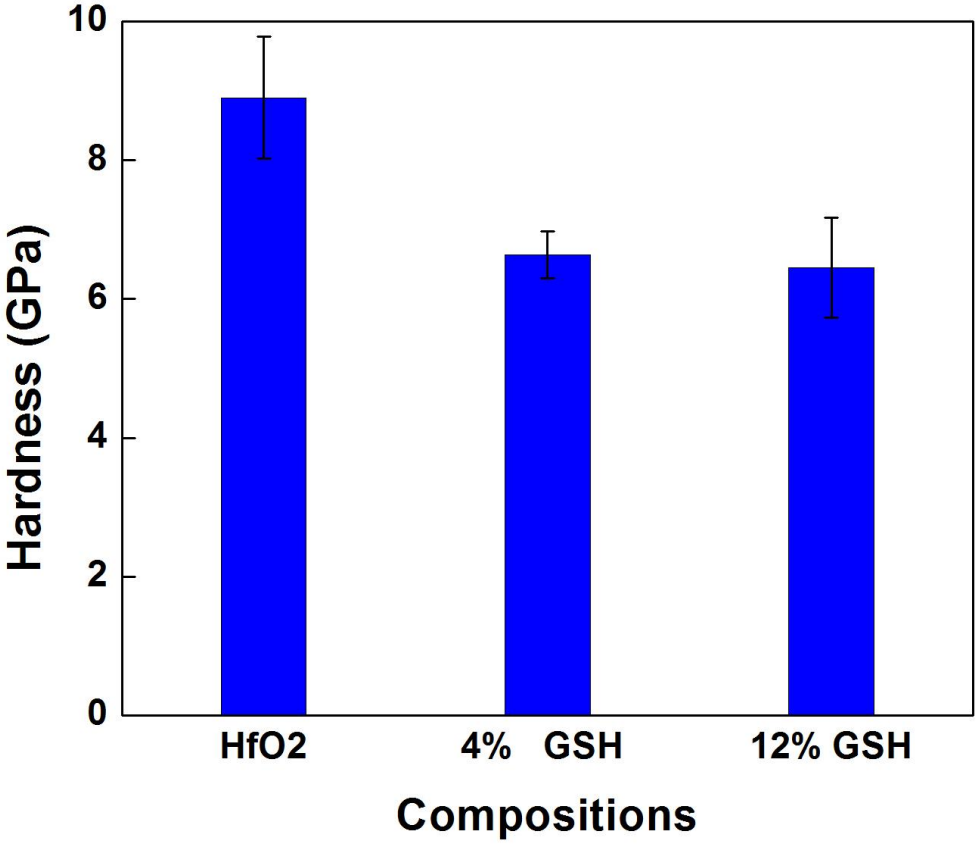

Figure 6.10: Hardness of different coating compositions

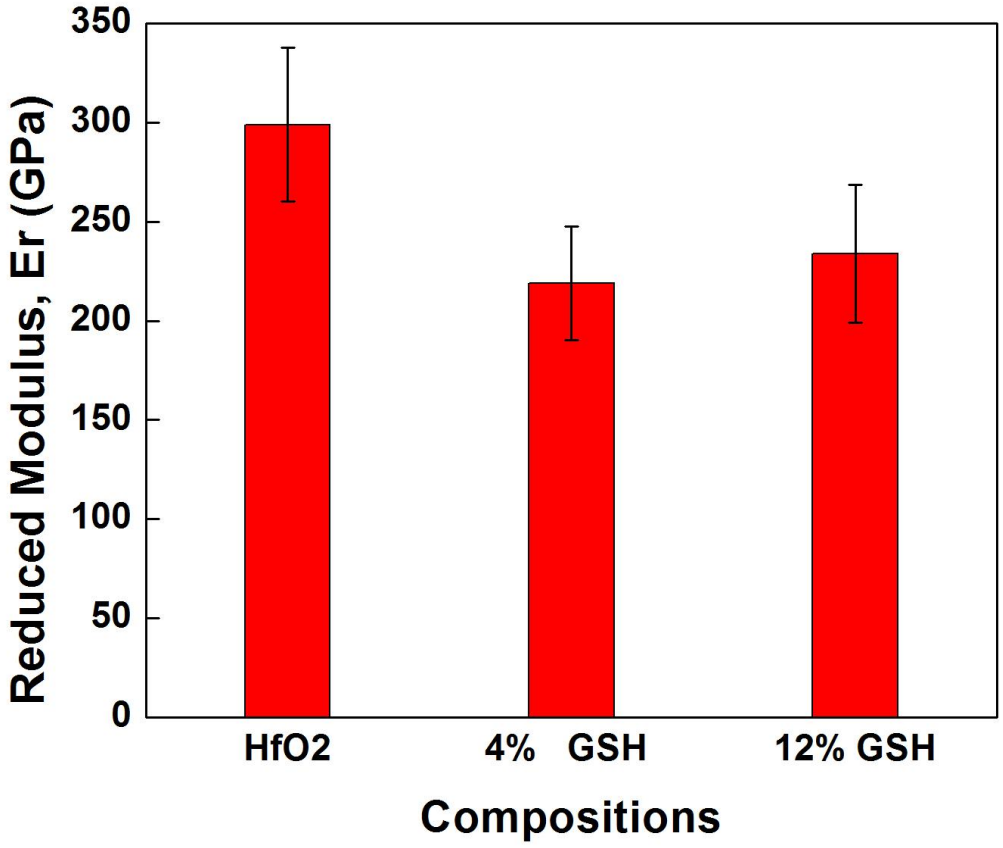

Figure 6.11: Reduced modulus of different coating compositions

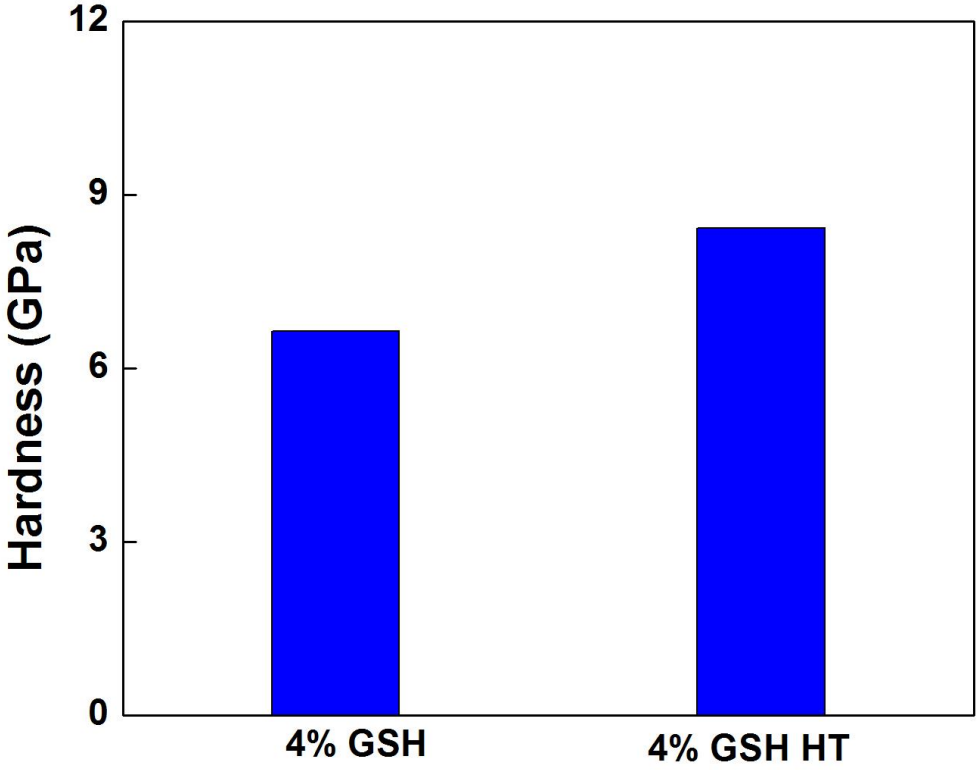

Figure 6.12: Hardness comparison for 4mol% gadolinia as deposited and heat treated coatings

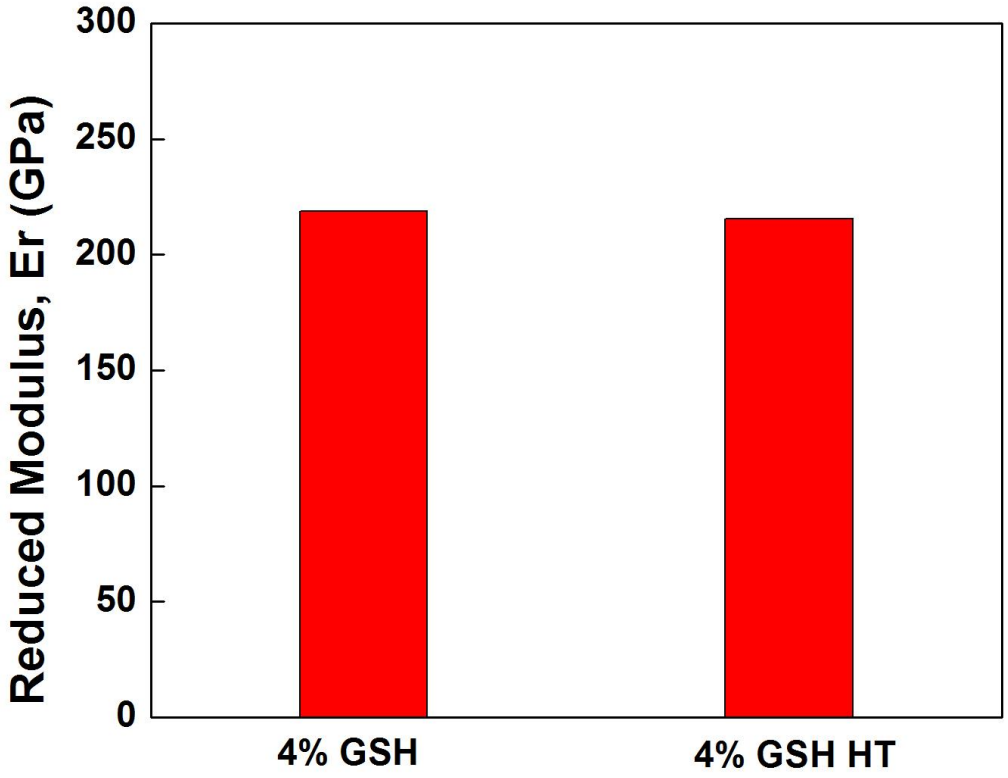

Figure 6.13: Reduced modulus comparison for 4mol% gadolinia as deposited and heat treated coatings

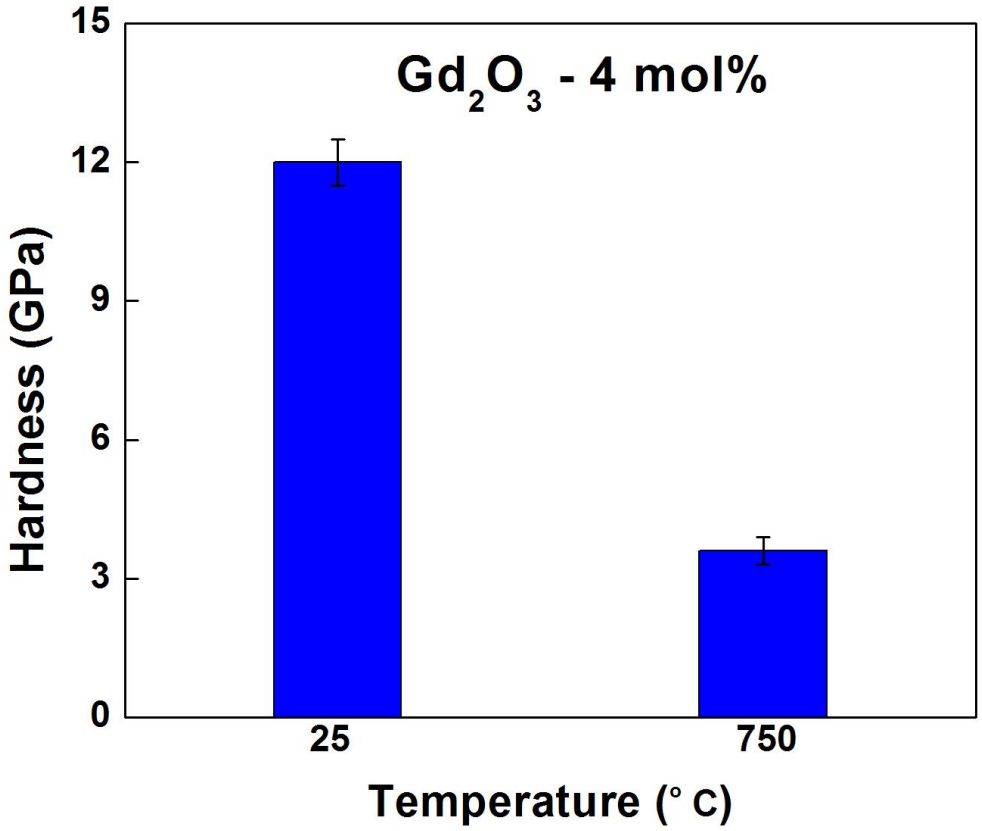

Figure 6.14: Hardness measurement for 4mol% gadolinia coatings at different temperatures

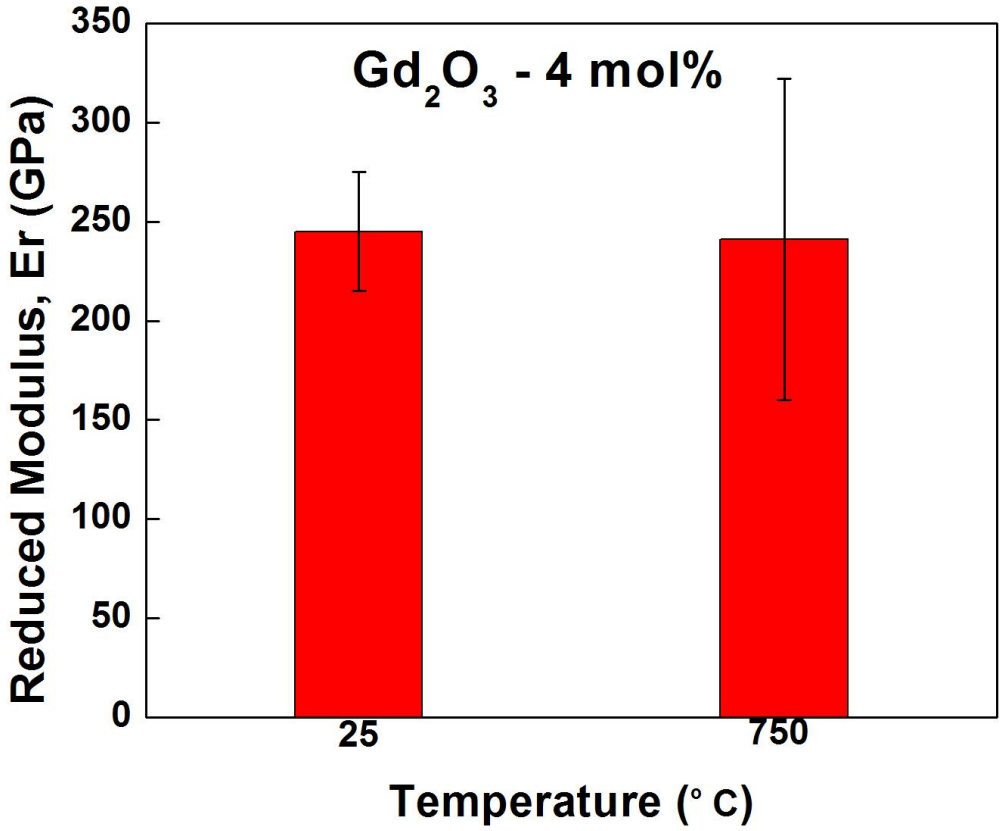

Figure 6.15: Reduced modulus of 4mol% gadolinia coatings at different temperatures

Nano impact testing was performed on the GSH coatings to understand their erosion resistance. The measurements were performed on the coatings deposited on Sapphire substrates at room temperatures. The obvious reason was the calibration readily available and sapphire can provide excellent mechanical toughness which facilitates such measurements and reliable information pertaining to the coating alone. The impacts were performed at loads of 10 mN and 15 mN, while the penetration depth of the indenter was measured as a function of time. There were four impacts every 4 s with a total of 75 impacts in a total of 300s duration, all at the same position on the coating surface. Between the impacts, the indenter was retracted to a distance of

10 μm before striking the surface of the coating. The coatings were tolerant; no damage was observed after initial impacts at a load of 10 mN. However, at 15 mN, cracking was observed in the GSH coatings with higher gadolinia content (as shown in Figures 6.16 and 6.17) after only a few impacts leading to a large final depth signifying a reduction in fatigue fracture resistance. We believe that this characteristic feature of the GSH coatings is mainly due to interface morphology, which is characterized by the tightly packed columns as can be seen from the cross sectional SEM images (Figure 6.7). Cracks induced parallel to the substrate in the columns upon impact propagate to the adjacent columns due to their close packed structure. On the contrary, when the coatings were subjected to heat treatment, their impact resistance has increased and the final depth after impact was reduced when compared to the untreated coatings (Figure 6.18). Although there was some initial cracking induced in the coatings, the final depth reduction could be due to inter-columnar spacing. This can be attributed to the rearrangement of atoms due to the additional energy imparted during the heat treatment. This rearrangement could have led to the spacing between the columns.

High temperature impact testing was also carried out on 4 mol% and 12 mol% gadolinia doped coatings to understand their fracture behavior. The testing was done at 750˚ C to understand the fracture mechanism at extreme temperatures and also again at room temperature post heating. Initially at room temperature, the coating cracked after less than 10 impacts leading to a large final depth. The cracking events can be confirmed by the sudden increase in depth from the curves. But, at 750˚ C the cracking behavior of the coating seemed much more ductile than brittle when compared to room temperature measurement. Although there are severe

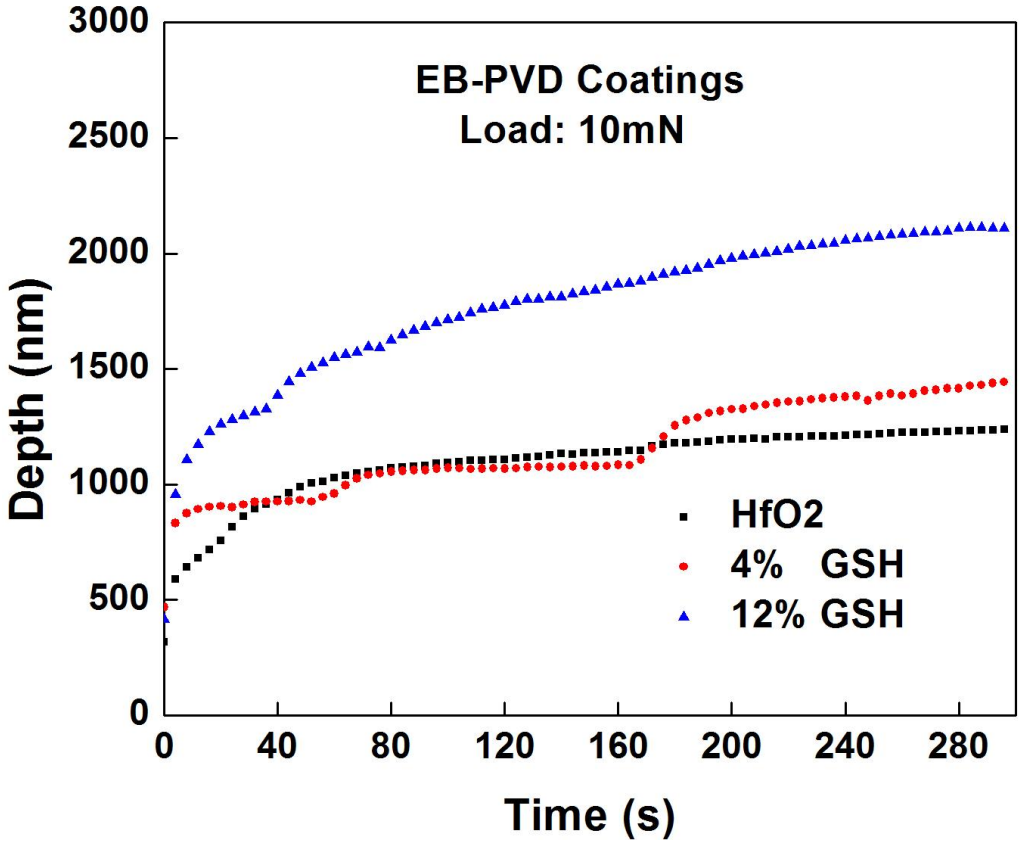

Figure 6.16: Impact testing at a load of 10mN on various coating compositions

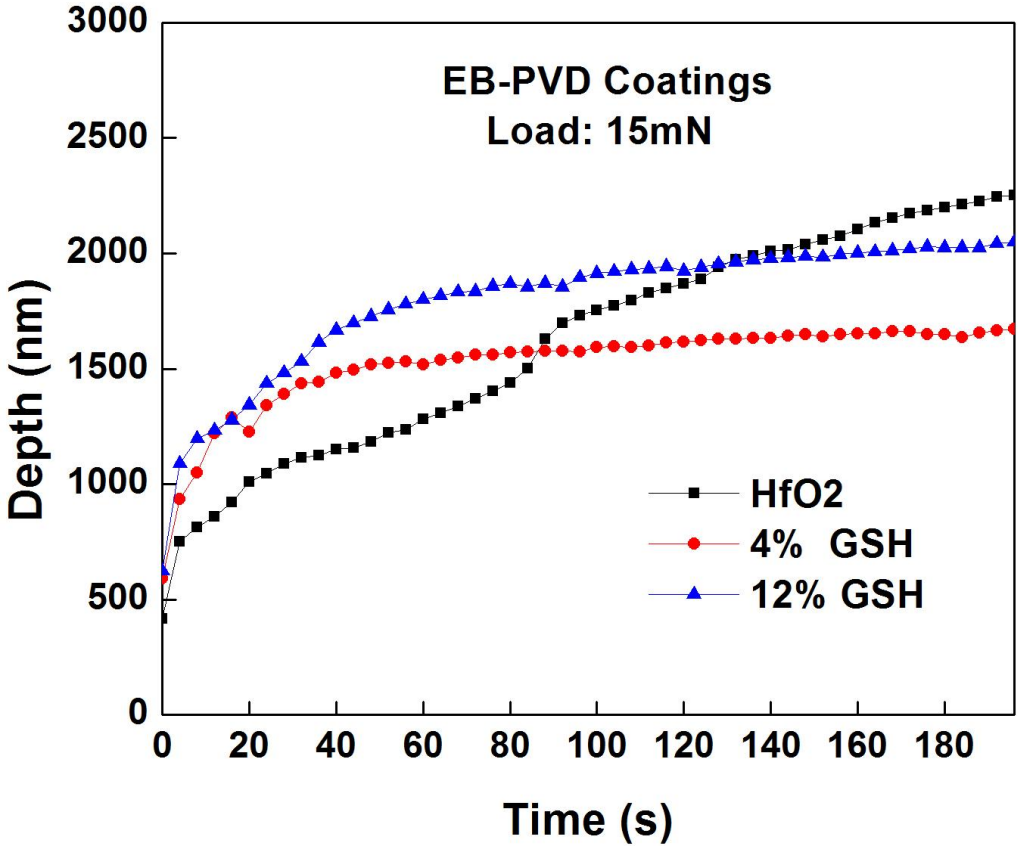

Figure 6.17: Impact testing at a load of 15mN on various coating compositions

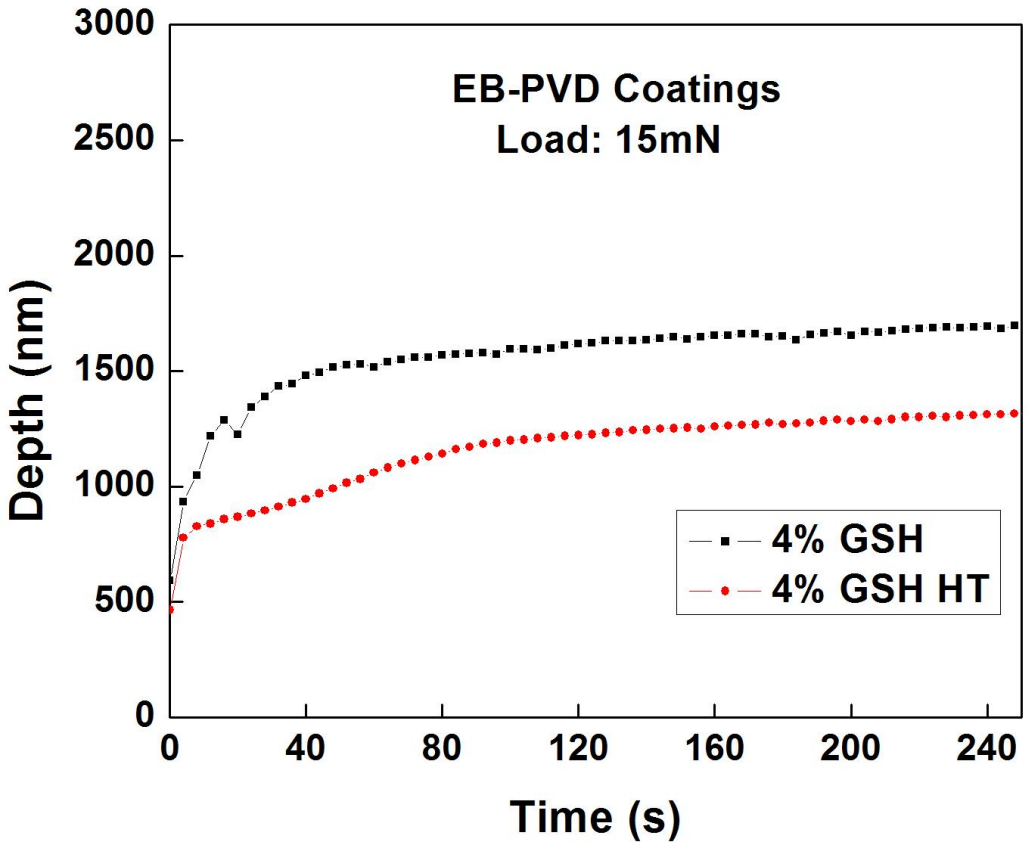

Figure 6.18: Impact testing at a load of 15mN on 4mol% gadolinia as deposited and heat treated coatings.

cracking events, the penetration depth was much less than at room temperature (as observed in Figures 6.19 and 6.20). This can be attributed to the softening of the coating surface leading to a reduction in the hardness which influences the fracture behavior. When the impact testing was performed again at room temperature upon post heating, the material tends to behave brittle again leading to large penetration depth compared to the high temperature measurement. This observation suggests that the effect of temperature is reversible and the change in coating behavior is mainly due to the changes in the mechanical properties rather than structural changes.

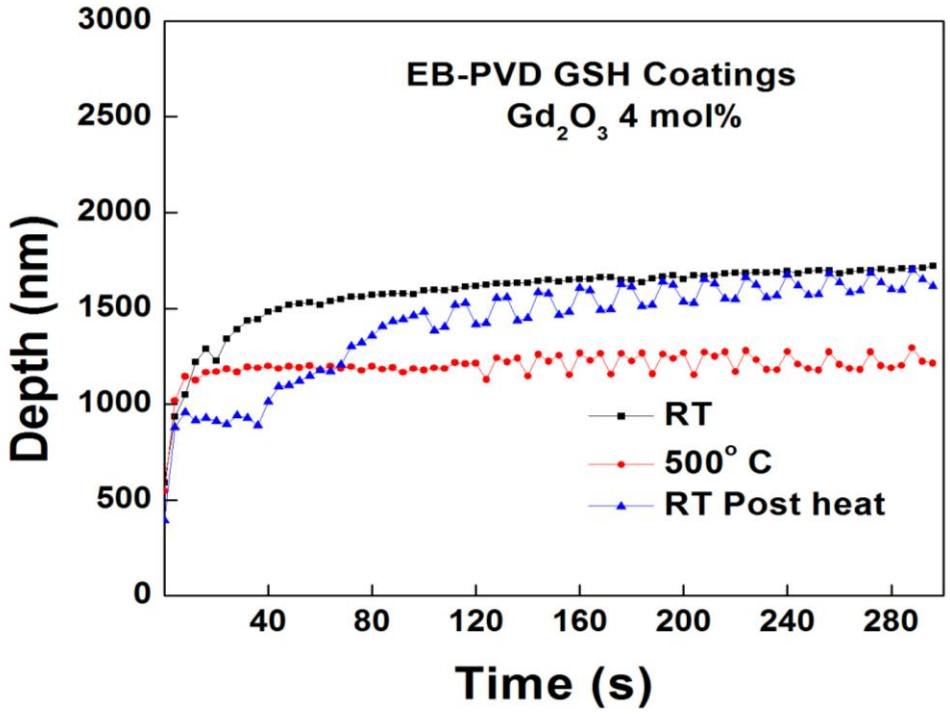

Figure 6.19: High temperature impact testing on 4 mol% gadolinia doped samples

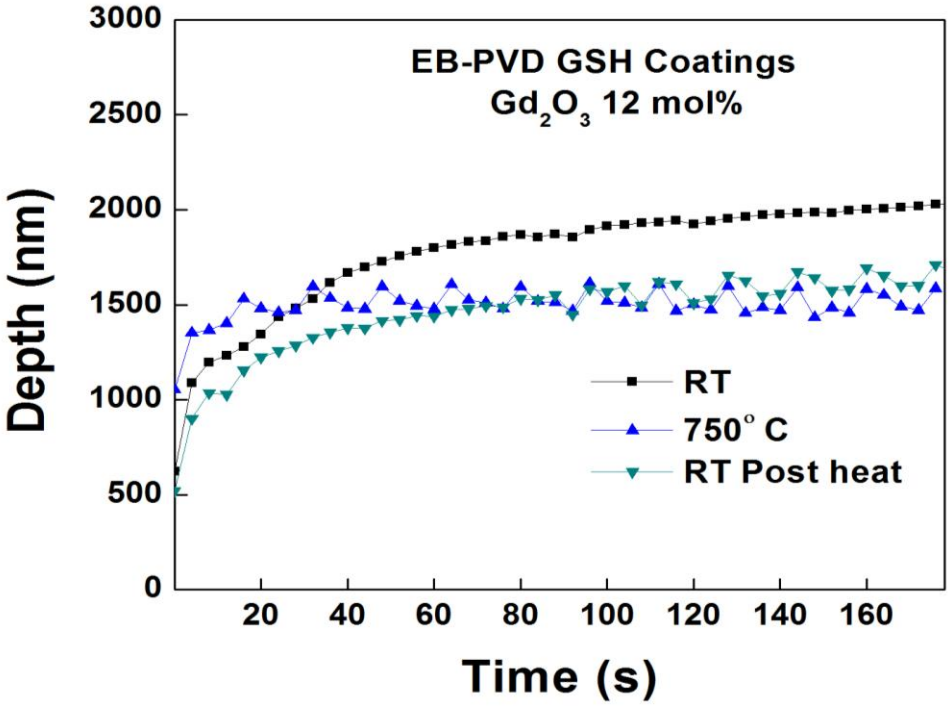

Figure 6.20: High temperature impact testing on 12 mol% gadolinia doped samples

6.5 THERMAL OXIDATION

The coatings were subjected to thermal oxidation at 900˚C for a total duration of 160 hr. The results obtained in thermal oxidation measurements are shown in Figures 6.21 and 6.22. The weight gain in both the samples was about 0.0162 gm after 160 hr of oxidation. This very low weight gain in the GSH samples is due to the Gd^{3+} ions diffusing through the oxide scale to the gas interface after prolonged oxidation through the grain boundaries. Due to its larger ionic radius, it inhibits the outward diffusion of alloy cations through the grain boundaries preventing further oxidation (21). The similar weight gain in both the samples indicates that the difference in the content of gadolinia is not high enough to notice a change in the amount of oxidation. When compared to the yttria doped hafnia samples which had a weight gain of 0.023 gm (Figure 6.23), the weight gain in gadolinia doped hafnia is initially high, but with the increase in oxidation time, the weight gain in gadolinia doped coatings is less than yttria stabilized coatings.

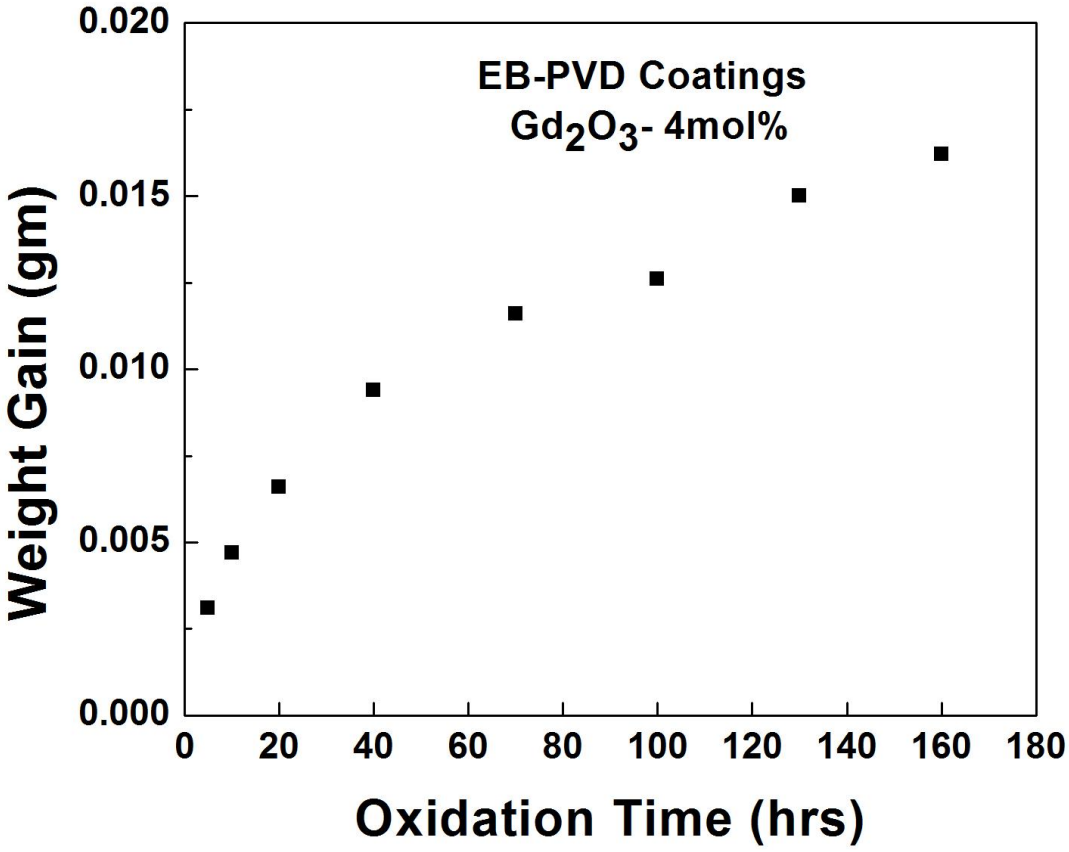

Figure 6.21: Weight gain of 4 mol% gadolinia doped coating

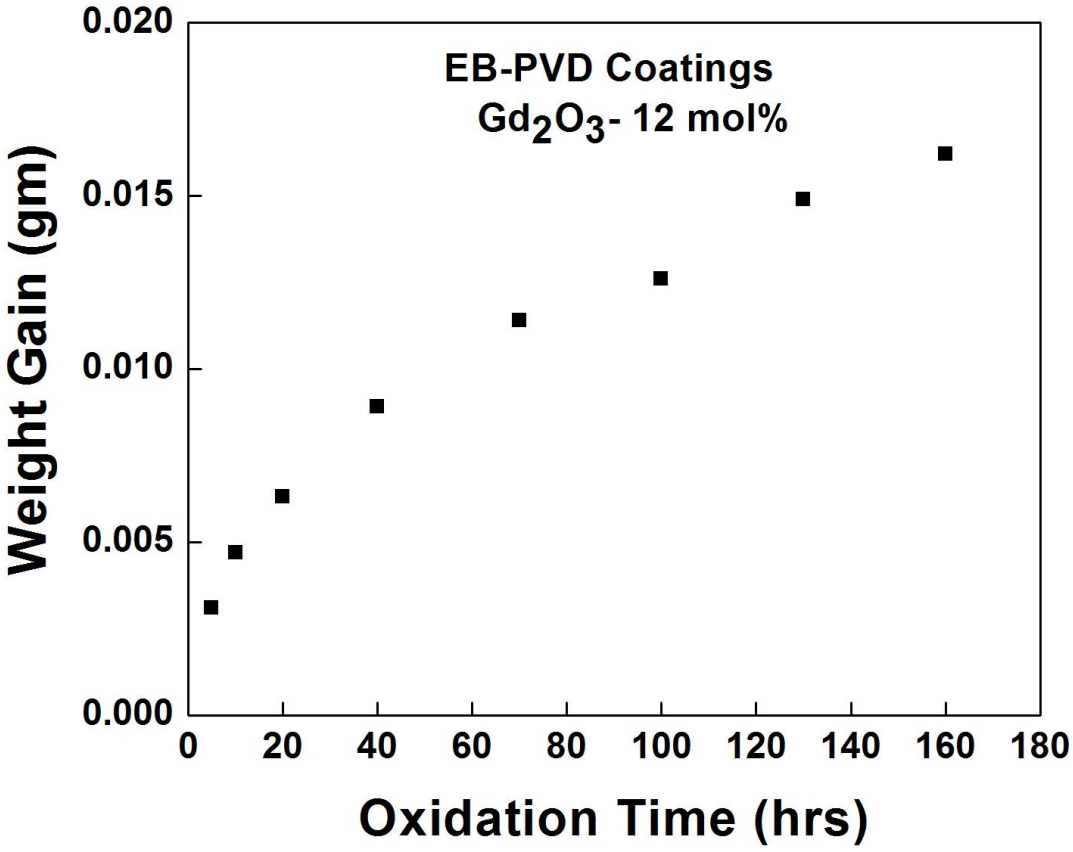

Figure 6.22: Weight gain of 12 mol% gadolinia doped coating

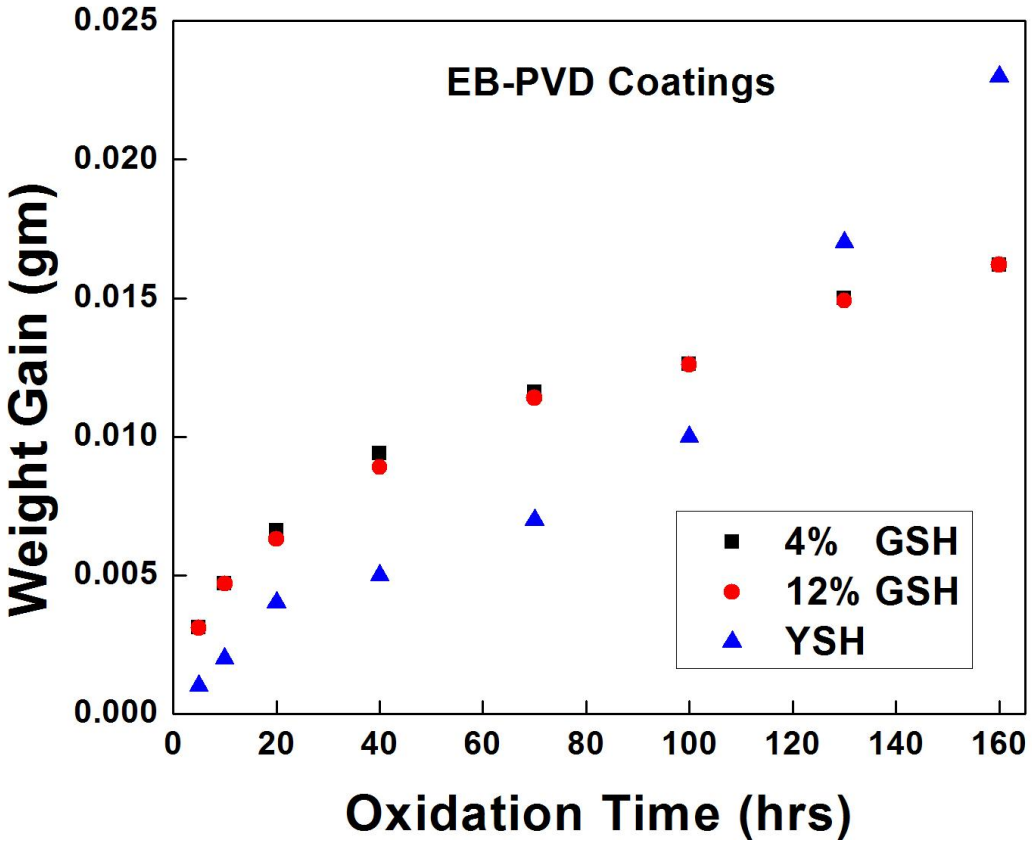

Figure 6.23: Comparison of oxidation in yttria doped hafnia and gadolinia doped hafnia coatings

6.6 THERMAL CYCLING

The coatings were subjected to a thermal cycling test, which constitutes 200 cycles at a temperature of 900˚ C for duration of one hour for each cycle. The temperature was chosen considering the operable limit of the Inconel substrate that was not coated completely, whose properties degrade when exposed to temperature beyond 983˚ C. The as deposited and annealed coatings of 4 and 12 mol% gadolinia doped hafnia coatings were used for testing to make a comparison.

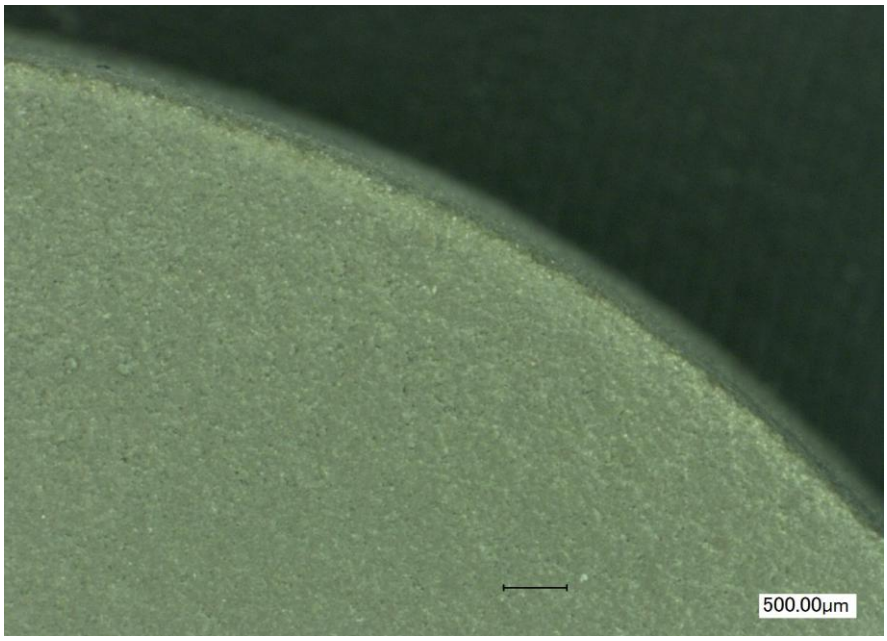

Figure 6.24: As deposited coatings before thermal cycling

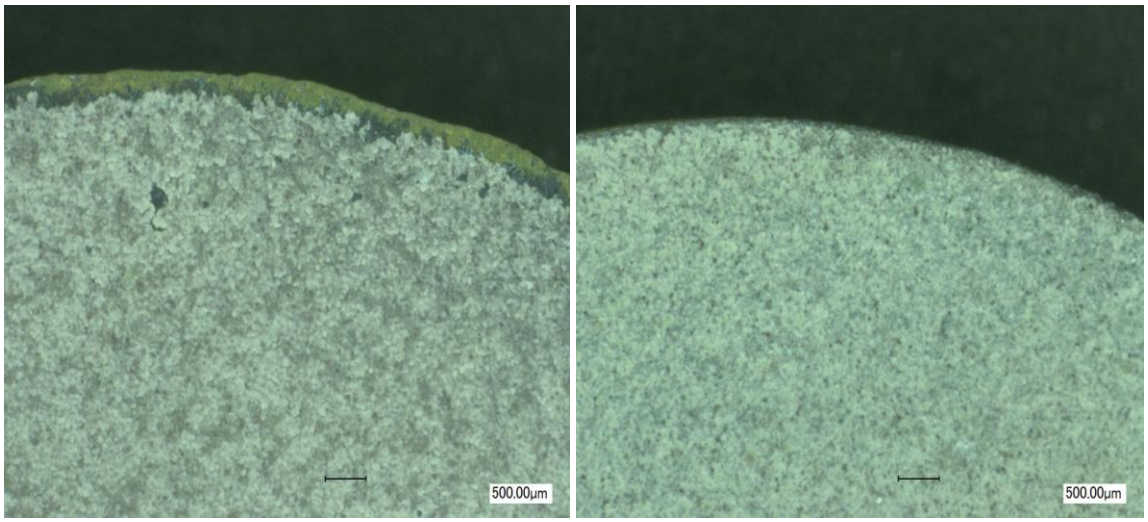

(a) (b)

Figure 6.25: Annealed coatings a) GSH 4mol% b) GSH 12mol% subject to 200 thermal cycles

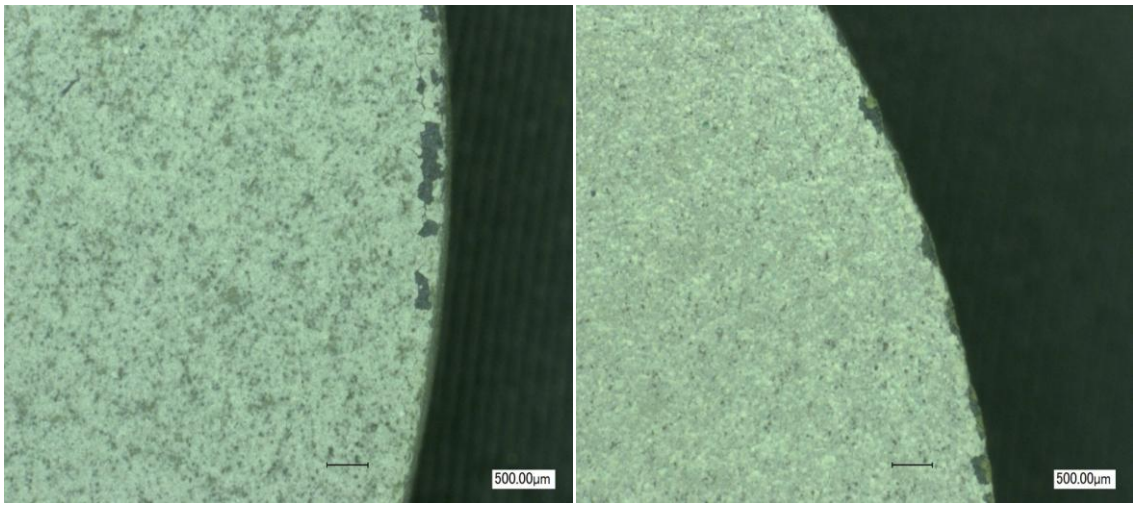

(a) (b)

Figure 6.26: As deposited coatings a) GSH 4mol% b) GSH 12mol% subject to 200 thermal cycles

A micrograph of the as deposited coating before cycling is provided for reference in Figure 6.24. It can be observed from Figure 6.25, that the annealed coating with 4 mol% gadolinia spalls more than the 12 mol% gadolinia sample. The same trend is observed in the as deposited coatings shown in Figure 6.26 but the spallation is quite less when compared to the annealed samples. This could be due to the low thermal expansion of the 4 mol% gadolinia when compared to the 12 mol% gadolinia which creates a mismatch with the thermal expansion of the substrate. The thermal expansion difference with change in percentage of gadolinia and hafnia has been reported by Dole et.al (46).

6.7 IMPEDANCE

Gadolinia doped hafnia and pure hafnia pellets were synthesized using standard ceramic method and were subjected to thermal cycling. Impedance measurements and analysis was performed to derive an understanding of the thermal oxidation behavior from a different perspective. Specifically, the impedance measurements are expected to provide insights into the micro or atomistic processes involved in terms of both oxidation resistance and effect of

morphology in terms of grain versus grain boundary contributions. The complex impedance data of GSH samples are shown in Figure 6.27 and 6.28. The data as a function of number of thermal cycles for various compositions of GSH are presented. For the first thermal cycle, the impedance is noted to increase with increasing gadolinia content in hafnia. The observed increasing trend in impedance can attributed mainly to the chemical nature i.e., incorporation of Gd^{3+} ions into HfO_2 (Hf^{4+} ions). The Gd^{3+} ions have introduced defects that increase the resistance of the bulk. But, when the concentration of gadolinia had gone up to 38%, the impedance was lower than pure hafnia. This may be due to the signature effect of Gd^{3+} ions dominating the Hf^{4+} ions in HfO_2. On the contrary, when the measurements were taken after exposure to 100 thermal cycles, it can be noticed that the impedance of 38 mol% pellets is higher than pure hafnia. Also, the impedance of 12 mol% is higher than 4 mol% indicating the influence of a large number of Gd^{3+} ions although the overall impedance in all the pellets has been reduced when compared to the pellets exposed to a single thermal cycle.

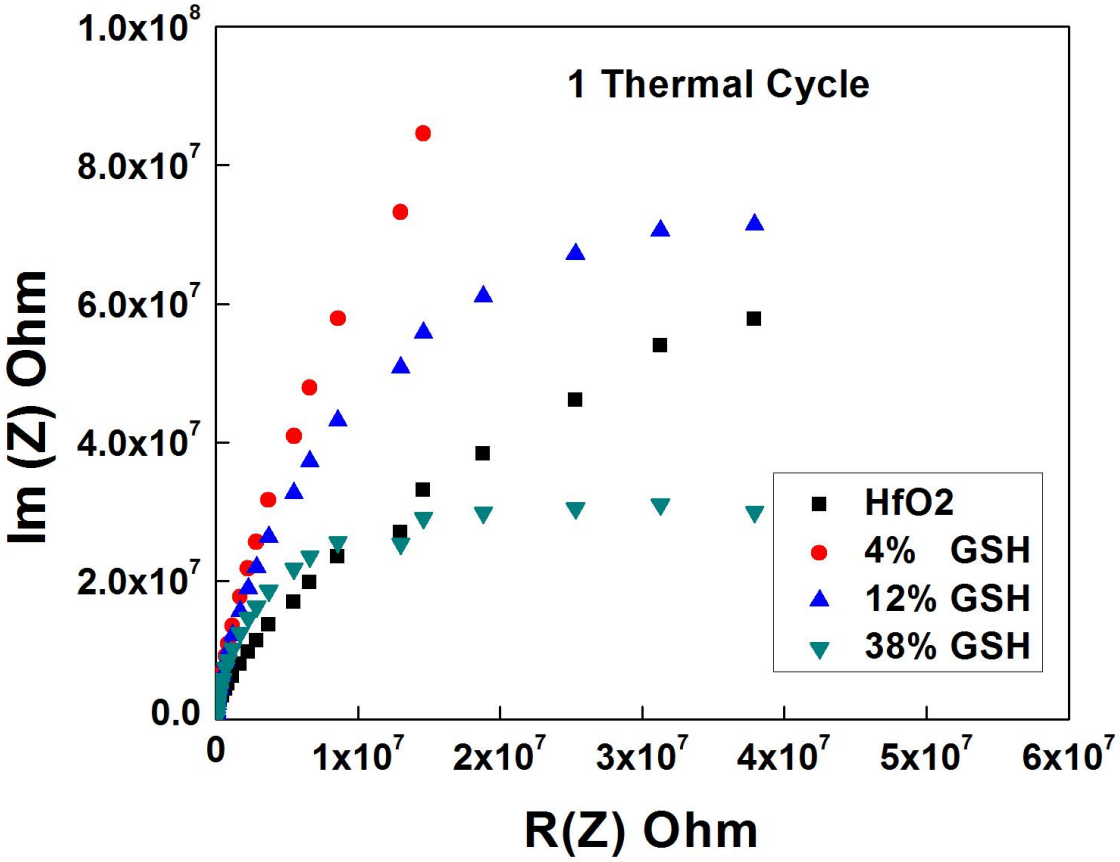

Figure 6.27: Complex plane plot for bulk materials after one thermal cycle

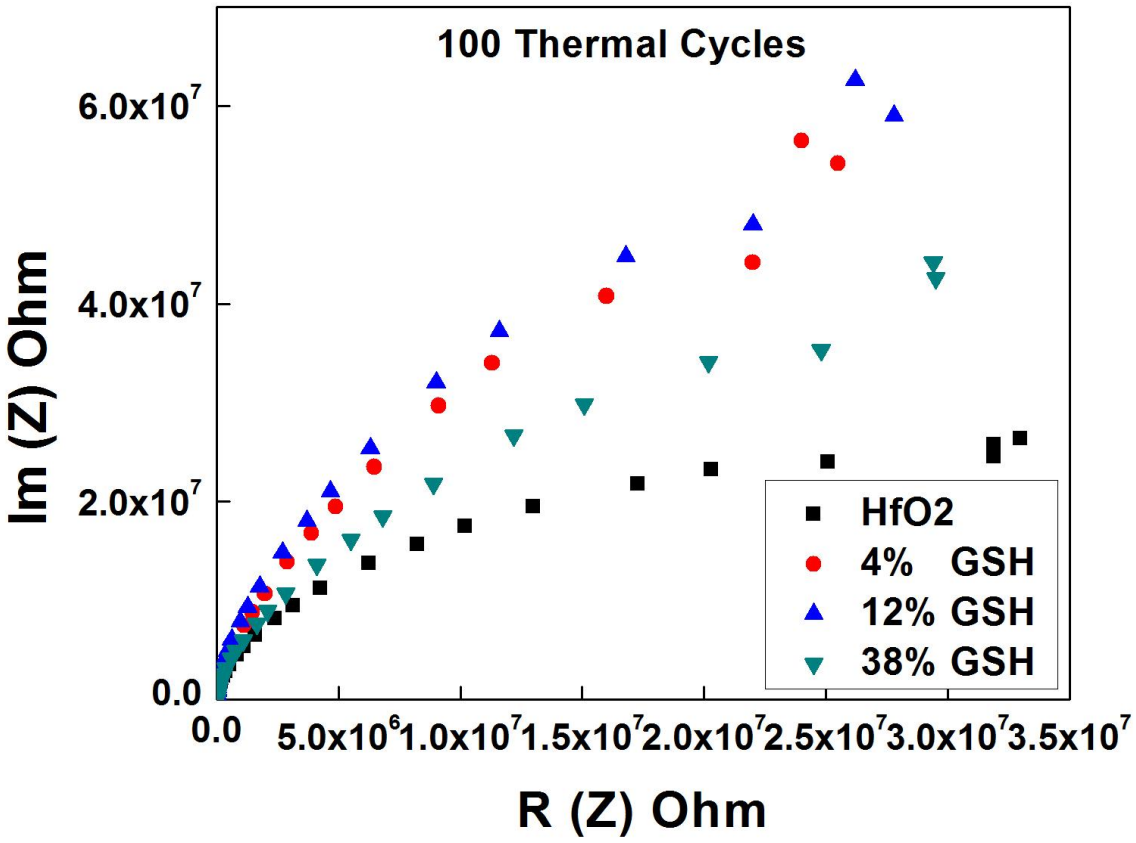

Figure 6.28: Complex plane plot for bulk materials after 100 thermal cycles

6.8 THERMAL PROPERTIES

Specific heat measurements were performed on the sintered pellets using the differential scanning calorimetry. The measurements were performed from room temperature up to a temperature of 1000˚ C as shown in Figure 6.29. From the plot, it can be noticed that with the increase in gadolinia content the specific heat values are decreasing at high temperatures. This can be attributed to the oxygen vacancies introduced into the bulk material due to the addition of gadolinia which play a significant role in increased phonon scattering. These are structural vacancies in the hafnia due to charge compensation of Gd^{3+} ions substituting for Hf^{4+} ions.

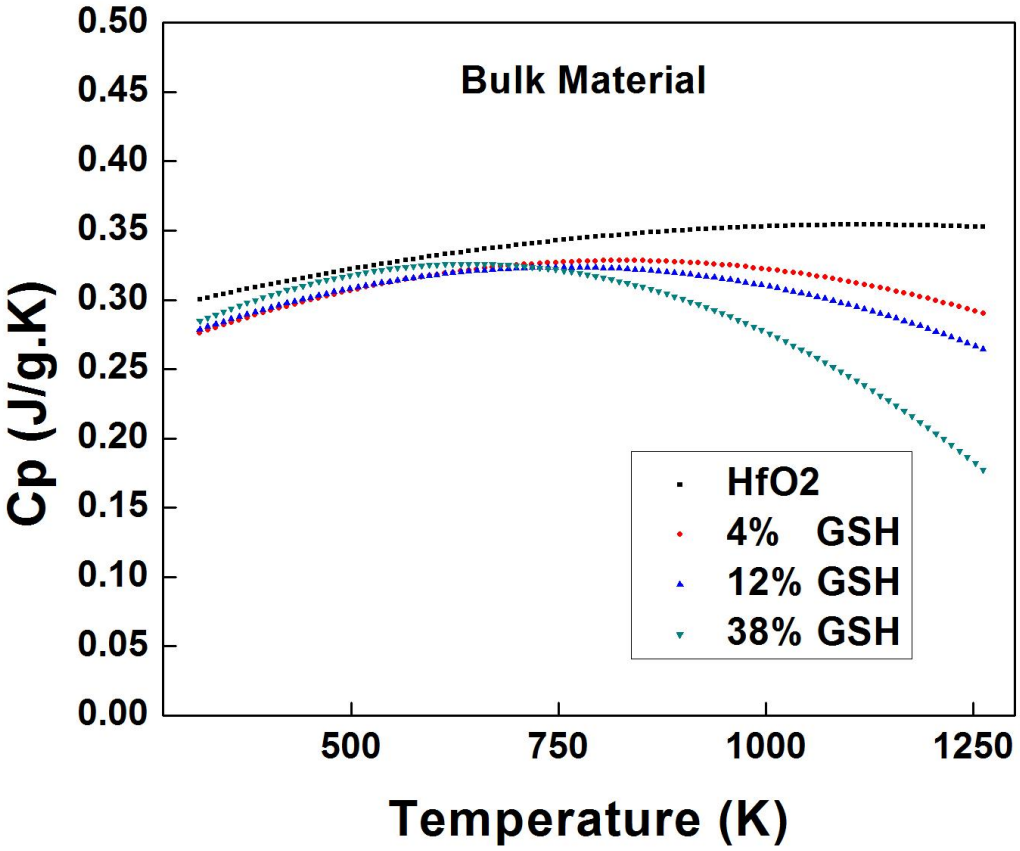

Figure 6.29: Specific heat measurements on different bulk hafnia and gadolinia doped hafnia compositions

6.9 Finite Element Analysis

The finite element models of YSZ and YSH coatings were run through 75 thermal cycles. Comparing the stresses at the interface between the YSZ-bond coat and YSH-bond coat, we notice that there are higher stresses developed in the YSH interface than at the YSZ interface. This can attributed to the fact that YSH has a higher modulus of elasticity when compared to YSZ top coat. This has been confirmed from the work done by He *et al* (47) where an increase in modulus of elasticity leads to higher stresses. Even though there are higher stresses in YSH when compared to YSZ coatings, YSH coatings are expected to have a higher tendency to sustain more stresses than YSZ. This can be attributed to the phase transformations that take place in these two coatings. Zirconia coatings transform from t' to tetragonal at 1200 °C leading

to a change in volume which introduces cracks that lead to spallation, while on the other hand hafnia coatings undergo phase transformations only at 1700 °C which is far beyond the operating temperatures (12).

The stress distribution at interface layers in the YSZ and YSH coatings at different thermal cycles are shown in Figures 6.30 and 6.31. The oxide layer grows from one micron during the first cycle to three microns by the end of the 75^{th} cycle, during which higher stresses are developed due to the volumetric expansion and thermal expansion mismatch. An increase in volume of the oxide layer is likely to put additional surface pressure at the coating interface which can also be an important factor for the delamination (48). Tensile stresses were induced in the top coat material and were found to increase with an increase in thermal cycling for both the YSZ and YSH coatings. These results were also observed in the work of He (47). We observe that as the oxide layer grows, higher stresses are induced in it when compared to the top coat and bond coat. We can also notice there are higher stresses at the free edge between the TGO and top coat interface. This higher stress can be attributed to the difference in thermal expansion coefficient of the TGO and top coat and also by the edge delamination effect which is a mode II cracking phenomenon when the film is in shear. This is evident from the shear stress distribution at the interfaces shown in Figure 6.32 This effect can be even more predominant if there was an interface roughness (49) introduced in the model at the interface. Based on the stress distribution results, a simple damage evolution model along with damage initiation criterion model was used to understand the degradation at the interfaces. The preliminary work, (not shown here) involved verification models where a single element for each layer was used instead of the multiple elements and subjected to thermal loading. The damage was observed in the TGO layer under

static conditions but not under thermal cycling conditions. This needs the development of a separate user defined subroutine which includes the growth model into the damage model.

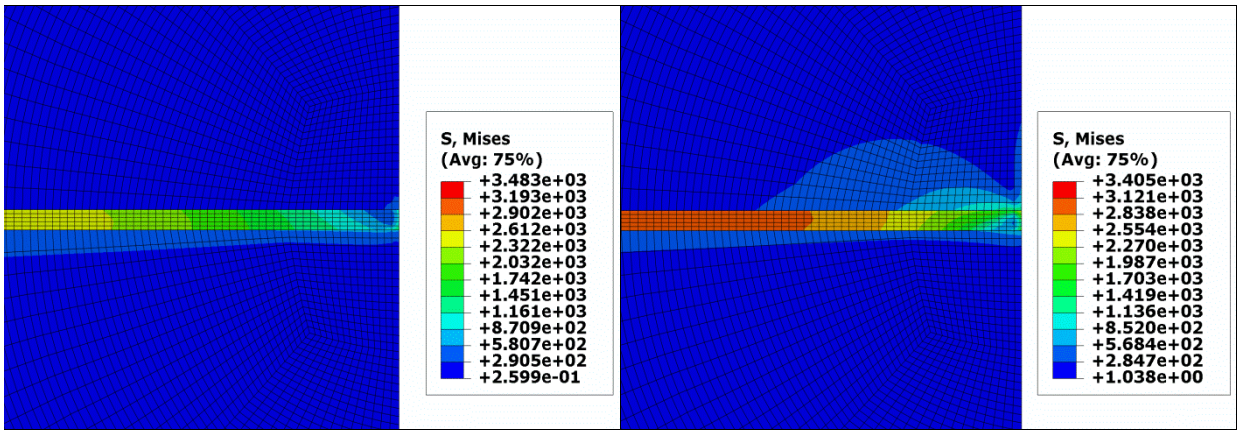

Figure 6.30: Stress distributions at the interfaces for YSZ (left) and YSH (right) coatings after one cycle

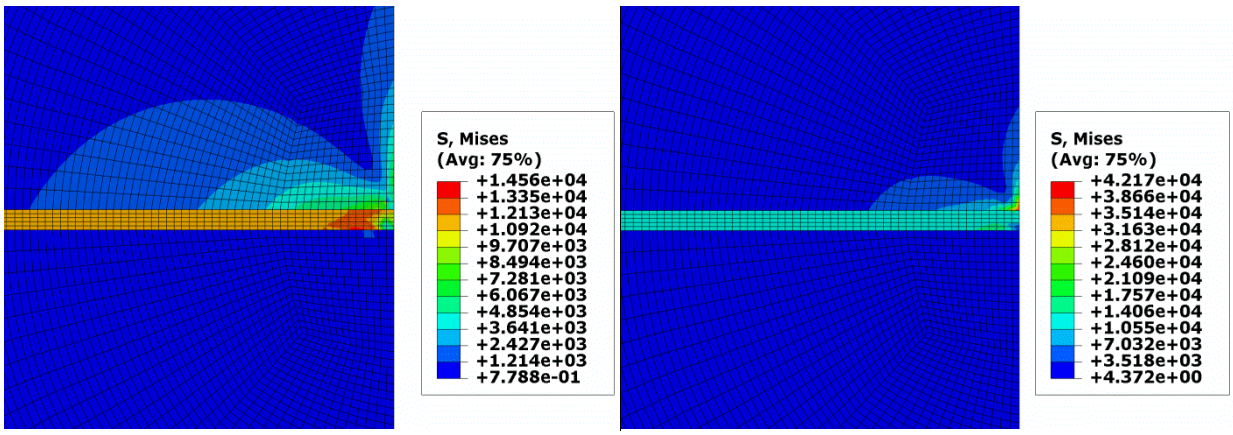

Figure 6.31: Stress distributions at the interfaces for YSZ (left) and YSH (right) coatings after 75 cycles

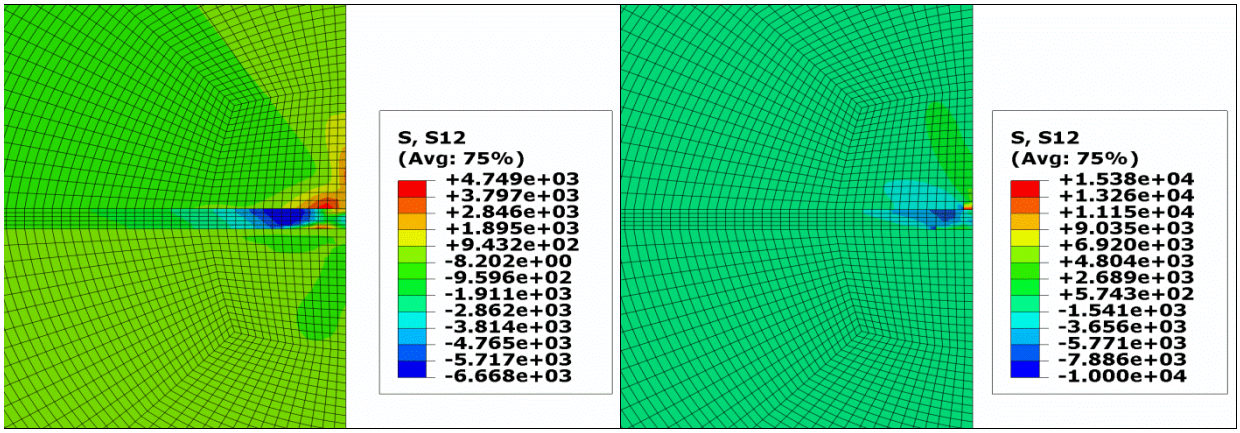

Figure 6.32: Shear stress distribution in YSZ (left) and YSH (right) coatings

Chapter 7: Conclusions

Gd_2O_3 - HfO_2 coatings were fabricated using electron beam physical vapor deposition (EB-PVD) technique onto Inconel-738 and sapphire substrates. XRD analysis of the coatings confirms the stabilization of the high temperature cubic phase of hafnia at room temperature with the addition of gadolinia. Morphology and cross sectional analysis show the columnar structure of the coatings which is a signature of the EB-PVD coatings. Mechanical characterization of the coatings shows a reduction in the hardness and reduced fracture resistance with increasing gadolinia content. High temperature nanoindentation shows a change in the mechanical properties of the coatings when exposed to high temperatures. Impact testing at room temperature and high temperature give a profile of the cracking phenomenon in the coatings. Oxidation tests carried out on the coatings at a temperature of 900˚ C for a total of 160 hours showed a remarkable improvement in oxidation resistance when compared to the YSH coatings due to the presence of gadolinia. Thermal cycling of the coatings at 900˚ C for 200 cycles leads to a high spallation in the annealed 4 mol% gadolinia coatings than the as deposited coatings due to the thermal expansion mismatch. Bulk hafnia and gadolinia doped hafnia pellets were prepared to understand the thermal oxidation behavior and addition of gadolinia using the impedance characteristics of the material. Finite element models were also developed to understand the interfacial stress distribution in the YSZ and YSH coatings when subjected to thermal cycling.

Chapter 8: Future Work

Based on the observations made from this work, the scope for future work is as follows.

1. Thermal conductivity measurements can be performed on the coatings at very high temperatures using the laser flash technique.
2. The coatings can be tested in a combustion chamber to study the effect of hot gas exposure on the microstructure and properties.
3. Corrosion testing can be performed by depositing salt on the surface of the coatings and expose to high temperature.
4. User defined subroutine can be developed to model damage in the coating using finite element analysis.

References

1. G. W. Goward**,** "Progress in coatings for gas turbine airfoils," *Surface and Coatings Technology*, **108-109**, 73-79 (1998).
2. H. B. Xu, S. H. Gong and L. Deng, "Preparation of thermal barrier coatings for gas turbine blades by EB-PVD," *Thin Solid Films*, **334**, 98 (1998).
3. R. A. Miller, "History of thermal barrier coatings for gas turbine engines," *Engineering Conferences International* (2007).
4. K. H. Stern, "Metallurgical and ceramic protective coatings," Chapman and Hall (1996).
5. P. W. Schilke, "Advanced gas turbine materials and coatings," GE Energy, Schenectady, NY.
6. N. P. Padture, "Thermal barrier coatings for gas turbine engine applications," *Science*, **296**, 280 (2002).
7. J. R. Nicholls, K. J. Lawson, A. Johnstone and D. S. Rickerby, "Methods to reduce the thermal conductivity," *Surface and Coating s Technology*, **151-152**, 383 (2002).
8. D. S. Rutman and Y. S. Toropov, "High temperature zirconium dioxide base materials," *Moscow: Metallurgy*, 137 (1985).
9. D. R. Clarke and S. R. Phillpot, "Thermal barrier coating materials," *Materials Today*, **8**, 22 (2005).
10. X. Q. Cao, R. Vassen and D. Stover, "Ceramic materials for thermal barrier coatings," *Journal of European Ceramic Society*, **24**, 1 (2004).
11. Z. Xu, L. He, X. Zhong, R. Mu, S. He and X. Q. Cao, "Thermal barrier coating of lanthanum zirconium ceramic composite oxide made by electron beam physical vapor deposition," *Journal of Alloy Compounds*, **478**, 168 (2009).
12. J. Wang, H. P. Li and R. Stevens, "Hafnia and hafnia toughened ceramics," *Journal of Material Science*, **27**, 5397 (1992).
13. C. F. Grain and W. J. Campbell, "Thermal expansion and phase inversion of six refractory oxides," *US Bureau of Mines report of Investigation*, 5982 (1962).
14. R. C. Gravie and S. K. Chan, "Stability limits in the monoclinic-tetragonal transformations of zirconia," *Physica B*, **150**, 203 (1988).
15. K. Matsumoto, Y. Itoh and T. Kameda, "EB-PVD process and thermal properties of hafnia based thermal barrier coatings," *Science and Technology of Advanced Materials*, **4**, 153 (2003).
16. N. P. Padture and Maurice Gell, "Advanced thermal barrier coatings for industrial gas turbine engines," U.S Department of Neergy (2003).
17. A. Portinha,V. Teixeira, J. Carneiro, M. F. Costa, N. P. Barradas and A. D. Sequeira, "Stabilization of ZrO_2 PVD coatings with Gd2O3*," Surface and Coatigns Technology*, **188**, 107 (2004).
18. P. G. Klemens, "Thermal conductivity of solids," Academic Press (1969).
19. M. J. Maloney, "Thermal barrier coating system and materials," *US6924040B2* United States.
20. C. K. Roy, M. Noor A Alam, A. R. Choudhuri and C. V. Ramana, "Synthesis and microstructure of Gd_2O_3 doped HfO_2 ceramics," *Ceramic International*, **38**, 1801 (2012).

21. Lalgudi Venkataramana Ramanathan, Marina. F. Pillis and Stela Maria C. Fernandes, "Role of rare earth oxide coatings on oxidation resistance of chroma-forming alloys," *Journal of Material Science*, **43**, 530 (2008).
22. F. Cernuschi, L. Lorenzoni, S. Capelli, C. Guardamagna, M. Karger, R. vaben, K. Von Niessen, N. Markocsan, J. Menuey and Carlo Giolli, "Solid particle erosion of thermal spray and physical vapour deposition thermal barrier coatings," *Wear*, **271**, 2909 (2011).
23. R. Wellman, M. Deakin and J. Nicholls, "The effect of TBC morphology on the erosion rate of EB PVD TBCs," *Wear*, **258**, 349 (2005).
24. R. Wellman and J. Nicholls, "On the efect of ageing on the erosion of EB-PVD TBCs," *Surface and Coatings Technology*, **201**, 2140 (2006).
25. R. Steenbaker, R. G. Wellman and J. R. Nicholls, "Erosion of gadolinia doped EB-PVD TBCs," *Surface and Coatings Technology*, 201, 2140 (2006).

26. D. S. Almeida, C. R. M. Silva, M. C. A. Nono and A. A. C. Cairo "Thermal conductivity investigation of zirconia co-doped with yttria and niobia EB-PVD TBCs," *Materials Science and Engineering*, **443**, 60 (2007).

27. Xiao Huang, Dongmei Wang, Mario Lamontagne, and Christian Moreau, "Experimental study of metal oxides co-doped yttria stabilized zirconia," *Materials Science and Engineering B*, 149, 63 (2008).

28. D. E. Wolfe, J. Singh, R. A. Miller, J. I. Eldridge and Dong Ming Zhu, "Tailored microstructure of EB-PVD 8YSZ thermal barrier coaings with low thermal conductivity and high thermal reflectivity for turbine applications," *Surface and Coatings Technology*, **190**, 132 (2005).

29. Xuan Zheng, D. G. Cahill and Ji-Cheng Zhao, "Thermal conductivity imaging of thermal barrier coatings," *Advanced Engineering Materials*, **7**, 7 (2005).

30. D. G. Cahill, "Thermal conductivity measurement from 30 to 750K: the 3 omega method," *Review of Scientific Instrumentation*, **61**, 802 (1990).

31. H. Wang, H. Hu and X. Xu, "Photo-acoustic measurement of thermal conductivity of thin films and bulk materials," ASME, **123**, 138 (2001).

32. Kazuhiro Ogawa, Dorian Minkov, Tetsuo Shoji, Minoru Sato and Hideo Hashimoto, "NDE of degradation of thermal barrier coating by means of impedance spectroscopy," *NDT & E International*, **32**, 177-185 (1999).

33. Zhang Dan Hua, Guo Hong Bo and Gond Sheng Kai, "Impedance spectroscopy study of high temperature oxidation of Gd2O3-Yb2O3 codoped zircnoia thermal barrier coatings," *Transactions of Nonferrous Metals Society of China*, **21,** 1061-1067, 2011.

34. J. Singh and D. E. Wolfe, "Nano and macro-structured component fabrication by electron beam physical vapor deposition (EB-PVD)," *Journal of Materials Science*, **40**, 1 (2005).

35. W. C. Oliver and G. M. Pharr, "Measurement of hardness and elastic modulus by instrumental indentation: Advances in understanding and refinements to methodology," *Journal of Materials Research*, **19**, 3-20 (2004).

36. Bharat Bhushan, "Handbook of Micro/Nano Tribology," CRC Press (1998).

37. K. Sfar, J. Aktaa and D. Munz, "Numerical investigation of residual stress fields and crack behavior in TBC systems," *Material Science and Engineering*, **A333,** 351 (2002).

38. M. Caliez, F. Feyel, S. Kruch and J. L. Chaboche, "Oxidation induced stress fields in an EB-PVD thermal barrier coating," *Surface and Coatings Technology*, **157**, 103 (2002).

39. M. Noor-A-Alam, S. K. Gullapalli, E. J. Rubio, A. Choudhuri and C. V. Ramana, "Enhanced stability of hafnia based coatings in hot gas environment," *RSC Advance*, **4**, 8224 (2014).

40. M. Ranjbar-Far, J. Absi, G. Mariaux and F. Dubios, "Simulation of the effect of material properties and interface roughness on the stress distribution in thermal barrier coatings using finite element method," *Materials Design*, **31**, 772 (2010).

41. H. Hooputra, H. Gese, H. Dell and H. Werner, "A comprehensive failure model for crash worthiness simulation of aluminum extrusions," *International Journal of Crashworthiness*, **9**, 449 (2004).

42. C. K. Roy, M. Noor-A-Alam, A. R. Choudhuri and C. V. Ramana, "Synthesis and microstructure of Gd_2O_3 doped HfO_2 ceramics," *Ceramics International*, **38**, 1801 (2012).

43. C. A. Johnson, J. A. Ruud, R. Bruce and D.Wortman, "Relationships between residual stress, microstructure and mechanical properties of electron beam-physical vapor deposition thermal barrier coatings," *Surface and Coatings Technology*, **108-109**, 80-85 (1998).

44. C. D. Wirkus and M. F. Berard, "Abradability and hradness in rare-earth-oxide stabilized hafnia," *Journal Materials Science*, **17**, 109-114 (1982).

45. Chang-Hoon Kim and Arthur H. Huer, "A high temperature displacement-sensitive indenter for studying mechanical properties of thermal barrier coatings," *Journal of Materials Research*, 19 (2004).

46. S. L. Dole and Jr, O. Hunter, "Elastic properties of some Gd2O3-HfO2 compositions," *Journal of Nuclear Materials*, **59**, 207-214 (1976).

47. M. Y. He, J. W. Hutchinson and A. G. Evans, "Simulation of stresses and delamination in a plasma sprayed thermal barrier system upon thermal cycling" *Material Science and Engineering*, **A345**, 172 (2003).

48. Z. A. Chaudhury, G. M. Nevarez, S. Q. Nusier and T. Ahmed, "Interfacial damage in EB-PVD thermal barrier coatings due to thermal cycling," *Material Science and Engineering*, **A231**, 34 (1997).

49. D. S. Balint and J. W. Hutchinson, “Mode II edge delamination of compressed thin films,” *Journal of Applied Mechanics*, **68**, 725 (2001).

Vita

Satya Kiran Gullapalli received his bachelor of science (B.S) in mechanical engineering from Jawaharlal Nehru Technological University (JNTU), India in 2008. He then joined the master's program in mechanical engineering at the University of Texas at El Paso (UTEP) and completed it in 2010. He worked on WO_3 thin film materials for gas sensor application in coal gasification systems for his master's thesis. After finishing his master's, Mr. Gullapalli joined the Energy Science and Engineering track in Environmental Science and Engineering doctoral program in 2010 and completed it in 2014. For his doctoral dissertation, he worked on Gd_2O_3 doped HfO_2 thermal barrier coatings for gas turbine applications. Mr. Gullapalli has a total of seven publications with a total of 139 citations. During his time in UTEP, he also worked as a teaching assistant for materials and manufacturing course for two years. He was one of the few graduate students who were awarded the Dodson's Research Grant by UTEP graduate school to meet their research goals during the academic year 2013-14. He was also a recipient of Texas Public Education Grant (TPEG) for International students.

This thesis/dissertation was typed by Satya Kiran Gullapalli.